Design and Characterization of Photoreactors for Environmental Applications

Lucas Siviero

Thesis submitted to the University of Ottawa
in partial Fulfillment of the requirements for the
Master of Applied Science in Chemical Engineering

Department of Chemical and Biological Engineering
Faculty of Engineering
University of Ottawa

© Lucas Siviero, Ottawa, Canada, 2026

Abstract

This work utilized a multiphysics approach combining computational fluid dynamics (CFD) and reduced-order modelling to perform intrinsic kinetic model fitting. Experimental results for the degradation of 4-chlorophenol (4-CP) on a flat plate photoreactor immobilized with TiO_2 were used. Using the fitted kinetic parameters, a simulation study examining both mass transfer effects and the absorbed radiation fields on a newly proposed surface-enhanced corrugated plate photoreactor (SECP) was conducted. CFD calculations using COMSOL Multiphysics were used to resolve the flow field as well as the local mass transfer fields by solving the incompressible continuity and Navier-Stokes equations along with the species transport equation with diffusion approximated by Fick's law. Monte Carlo ray tracing was used to solve the absorbed radiation fields on the reactive surface. A light-dependent Langmuir-Hinshelwood model was proposed as a suitable surface reaction rate. Nonlinear least squares regression was used to fit the kinetic parameters. Model predictions using the fitted parameters were found to agree well with the experimental data over a range of Reynolds numbers (431-5813) and light intensities (15-122 W m^{-2}). A linear light dependence was found to fit the experimental degradation optimally. Oxygen was found to have a linear dependence on the degradation rate, leading to a simplification in the kinetic model. A baseline corrugated plate photoreactor was modelled for comparison. A fully coupled model was solved which included laminar flow, species transport, radiation modelling, and the intrinsic kinetics to compute the degradation of 4-chlorophenol over this geometry. Comparison of diffusive and normal radiation models were also conducted. Results revealed a slightly higher degradation overall due to a more uniform radiation field allowing for more efficient use of regions with sufficient mass transfer rates. The SECP reactor fitted with cavities and protrusions was modelled. The SECP reactor using a moderate depth-to-diameter ratio of 0.2 yielded higher degradation performance overall compared to the unmodified surface. This small improvement in the total consumption under the dimpled surface is mostly attributed to a higher catalytic surface area rather than any benefits to the mass transfer or radiation field. At the low end of intensity, the rate is kinetically limited by the available photon flux. As the intensity increased, the rate transitioned into a mass-transfer-limited regime. Results from this study show potential in using surface modifications to improve photoreactors, but significant geometric optimization is required to optimize the surface mass transfer augmentation and absorbed radiation field.

Statement of Contributions

I, Lucas Siviero, hereby declare that I am the sole author of this thesis.

This thesis is written by me with editorial feedback from my supervisor, Dr. Zisheng Zhang, and my committee members, Dr. Jan Haelssig and Dr. Boguslaw Kruczek.

The experimental data used to perform the kinetic fitting correction was provided by my supervisor in his thesis titled: “Analysis of a Corrugated Plate Photoreactor”.

Acknowledgments

I would like to thank my supervisor, Dr. Zisheng Zhang, for his guidance and support throughout this project. I am expressly grateful for his encouragement, patience, and understanding throughout the writing of this thesis.

I would also like to thank my committee members, Dr. Jan Haelssig and Dr. Boguslaw Kruczek, for taking the time to read my thesis and provide feedback.

Table of Contents

1 Introduction 1
1.1 Motivation 1
1.2 Background 1
1.3 Current Limitations 2
1.4 Catalyst Deployment 2
1.5 Photoreactor Geometry 3
1.6 Protrusion/Cavity Reactor 4
1.7 4CP Degradation Kinetics 5
1.8 Research Goals 6
2 Model Development 8
2.1 Experimental Conditions 8
2.1.1 KE 8
2.1.2 SECP 9
2.2 Kinetic Model 13
2.3 Convective Mass Transfer 14
2.3.1 KE ..... **Error! Bookmark not defined.**
2.3.2 SECP ..... **Error! Bookmark not defined.**
2.4 Radiation Model 21
2.4.1 KE ..... **Error! Bookmark not defined.**
2.4.2 SECP 25
2.5 Computational Methods 26
2.5.1 KE ..... **Error! Bookmark not defined.**
2.5.2 SECP ..... **Error! Bookmark not defined.**
3 Results and Discussion 30
3.1 KE ..... **Error! Bookmark not defined.**
3.1.1 Flow Dependence 30
3.1.2 Radiation Field 32
3.1.3 Parameter Estimation 33
3.2 SECP ..... **Error! Bookmark not defined.**
3.2.1 Flow Structures 39
3.2.2 Radiation Profiles 46

3.2.3 Degradation Performance 50
4 Conclusions 56
5 References 58
6 Appendix – Meshing Strategies 62
6.1 Baseline Case 62
6.2 SECP 65

List of Figures

Figure 2.1. Isometric schematic of the flat plate photoreactor setup highlighting the lamp arrangement, acrylic cover, catalyst film, and flow direction. 8

Figure 2.2. A) Overall schematic of the corrugated plate photoreactor consistent with the dimensions given in Table 2.1. B) Dimensions of the triangular duct that makes up each corrugation. C) Zoomed-in depiction of the hemispherical surface modifications. D) Zoomed-in depiction of the tip truncation for meshing purposes. E) Planar surface showing the alignment of the surface modifications on a unit cell. 10

Figure 2.3. Geometric conventions for use in computing the fully developed velocity profile for an isosceles triangular duct. 18

Figure 2.4. Schematic for visualization of the boundary conditions for the base case and SECP reactor. 21

Figure 2.5. Spectral irradiance normal distribution produced by Zhang [21] based on the manufacturer data for the UV lamps 22

Figure 2.6. Spectral extinction coefficient of the UVT acrylic cover computed by Zhang [33] .. 22

Figure 2.7. Spectral absorption coefficient of the TiO2 film from Zhang [33] 23

Figure 2.8. Schematic outlining the radiation boundaries. 25

Figure 3.1. Kinetic fitting for the lumped parameter model under a perceived laminar flow regime. 30

Figure 3.2. Reynolds dependence of the lumped kinetic parameters. 31

Figure 3.3. LASREA field at the film surface for the flat plate geometry under diffuse radiation. 33

Figure 3.4. Model predictions compared with the experimental data showcasing the effect of Reynolds numbers on the degradation rate of 4-CP. Input intensity is 122 W m^{-2}. 34

Figure 3.5. 4-CP surface concentration profiles under various Reynolds numbers. Input intensity is 122 W m^{-2}. 35

Figure 3.6. Oxygen surface concentration profiles under various Reynolds numbers. Input intensity is 122 W m^{-2}. 35

Figure 3.7. Model predictions compared with the experimental data showcasing the effect of intensity on the degradation rate of 4-CP. Reynolds number is constant at 4314. 37

Figure 3.8. 4-CP surface concentration profiles under various intensities. Reynolds number is constant at 4313. 37

Figure 3.9. O2 surface concentration profiles under various intensities. Reynolds number is constant at 4313. 38

Figure 3.10. Contour showcasing the cross-sectional velocity profile for the unmodified triangular duct. The colour bar is the velocity magnitude in m s^{-1}. 40

Figure 3.11. Centerline velocity profile plotted with the analytical results computed by Equation 2.34..... 40

Figure 3.12. Normal diffusive flux profile in mol m^{-2} s^{-1} on one half of the symmetric film boundary. The max flux is manually set to 2E-07 mol m^{-2} s^{-1} to visually accentuate the entrance effect and the local differences caused by the geometry..... 41

Figure 3.13. 4-CP average mass transfer coefficients with varying Reynolds number. CFD and model predictions for a flat plate and corrugated plates with varying apex angles (defined using number of ducts) are presented..... 42

Figure 3.14. Flow streamlines for the near wall flow over a protrusion. Color bar gives the fluid velocity in m s^{-1}..... 43

Figure 3.15. Velocity streamline (Re = 1786) at the top dimple where the bulk velocity is near its maximum. A large recirculation zone is observed which pushes back the flow re-attachment point. Color bar gives the fluid velocity in m s^{-1}..... 44

Figure 3.16. Velocity streamline (Re = 1786) at the 4^{th} dimple where the bulk velocity has reused. A smaller recirculation zone is observed. The flow re-attachment point is now further down the dimple. Color bar gives the fluid velocity in m s^{-1}..... 45

Figure 3.17. Velocity streamline (Re = 1786) at the 9^{th} dimple where the bulk velocity is very low. No recirculation zone is observed. The flow follows the dimple curvature. Color bar gives the fluid velocity in m s^{-1}..... 45

Figure 3.18. LASREA contour for the base case under a diffuse radiation source. The color bar shows the reference LASREA magnitude in W m^{-2}..... 46

Figure 3.19. LASREA profile for the base case under a diffuse radiation source. 0.05 m corresponds to the top of the duct..... 47

Figure 3.20. LASREA contour for the base case under a normal radiation source. The color bar shows the reference LASREA magnitude in W m^{-2}..... 47

Figure 3.21. LASREA profile for the base case under a normal radiation source. 0.05 m corresponds to the top of the duct..... 48

Figure 3.22. Contour of the reference LASREA using a normal radiation source over the angled surface modified with protrusions. The axis angle is set so that the radiation rays enter parallel from left to right. The color bar shows the reference LASREA magnitude in W m^{-2}..... 49

Figure 3.23. Contour of the reference LASREA using a normal radiation source over the angled surface modified with dimples. The axis angle is set so that the radiation rays enter parallel from left to right. The color bar shows the reference LASREA magnitude in W m^{-2}..... 50

Figure 3.24. Total consumption of 4-CP for the baseline case under a diffuse radiation source as well as varying Reynolds numbers and input intensities..... 51

Figure 3.25. Total consumption of 4-CP for the baseline case under a normal radiation source as well as varying Reynolds numbers and input intensities..... 52

Figure 3.26. Total consumption loss of using a diffuse radiation source compared to a normal radiation source. 53

Figure 3.27. Total consumption of 4-CP for the dimple SECP case under a normal radiation source as well as varying Reynolds numbers and input intensities. 54

Figure 3.28. Normalized surface concentration (colour bar) on the catalyst film at the 100^{th} unit cell. Re = 1796 and I = 15 W m^{-2}. 54

Figure 3.29. Normalized surface concentration (colour bar) on the catalyst film at the 100^{th} unit cell. Re = 1796 and I = 122 W m^{-2}. 55

Figure 6.1. Structured quad mesh on the baseline geometry suitable for computing the laminar flow field. 62

Figure 6.2. Structured quad mesh on the baseline geometry suitable for resolving the diffusion boundary layer. 63

Figure 6.3. Mesh refinement plot for the average 4-CP mass transfer coefficient on the baseline geometry under the highest Re of 1700. 64

Figure 6.4. 4-CP average mass transfer coefficient compared to the Muzychka and Yovanovich model. 64

Figure 6.5. Mesh convergence plot for the recirculation volume within all the dimples modelled in the SECP reactor. 66

Figure 6.6. Flow mesh for the SECP 66

Figure 6.7. Mass transfer mesh for SECP 67

List of Tables

Table 2.1. Summary of reactor dimensions for the flat plate photoreactor..... 9
Table 2.2. Flow and radiation conditions for the flat plate. 9
Table 2.3. Summary of surface modification dimensions..... 12
Table 2.4. Summary of flow conditions tested for the SECP reactor..... 12
Table 2.5. Summary of the inlet stream properties. 16
Table 2.6. Summary of boundary conditions for the base case and SECP reactor. 21
Table 2.7. Film absorptivity, acrylic extinction coefficient, and irradiance for each discrete spectral band. 24
Table 2.8. Summary of radiative boundary conditions for the flat plate. 25
Table 2.9. Summary of radiative boundary conditions for the SECP and base case. 26
Table 3.1. Summary of Reynolds-dependent kinetic parameters for the lumped parameter model. 30
Table 3.2. Comparison of average mass transfer coefficient between the Muzychka and Yovanovich models versus the measured values from Zhang. 31
Table 3.3. Summary of the fitted kinetic parameters for the full LH model..... 33
Table 3.4. Summary of kinetic parameters for the reduced model. 39
Table 3.5. Pressure drop comparison to literature data for calculated pressure drops for the base case..... 43
Table 3.6. Comparison of dimple pressure drops to the base case. 46

Nomenclature

Latin

A	Cross-sectional area [m^2]
b	Triangular Duct Half Base [m]
b_{trunc}	Truncated Half Base [m]
C	4CP Molar Concentration [mol m^{-3}]
d_h	Hydraulic Diameter [m]
d	Cavity/Protrusion Diameter [m]
D	Mass Diffusivity [m^2 s^{-1}]
f	Fanning Friction Factor [-]
H_R	Reactor Height [m]
H_{trunc}	Truncated Height [m]
I	Intensity [W m^{-2}]
$\mathbf{I}$	Identity Matrix [-]
$\mathbf{J}$	Mass Diffusive Flux Vector [mol m^{-2} s^{-1}]
k_0	Forward Reaction Constant [mol m^{-2} s^{-1}]
k_0'	Reduced Forward Reaction Constant [m s^{-1}]
K_1	4CP Adsorption Constant [m^3 mol^{-1}]
K_2	O2 Adsorption Constant [m^3 mol^{-1}]
$\mathbf{K}$	Viscous Stress Tensor
k	Convective Mass Transfer Coefficient [m s^{-1}]
L_R	Reactor Length [m]
$\mathcal{L}$	Arbitrary Characteristic Length [m]
L_{hyp}	Triangular Duct Hypotenuse [m]
$\hat{M}$	Molecular Weight [kg $kmol^{-1}$]
N_D	Number of Cavities/Dimples [-]
N_t	Number of Channels [-]
N_u	Number of Unit Cells [-]
n	Light Dependence Parameter [-]
$\boldsymbol{N}$	Normal Vector [-]
O	Oxygen Molar Concentration [mol m^{-3}]
p	Wetted Perimeter [m]
P	Pressure [Pa]
Pt	Pitch [m]
Q	Volumetric Flowrate [m^{-3} s^{-1}]
q	Local Area Specific rate of Energy Absorption (LASREA) [W m^{-2}]
q_{ref}	Reference LASREA = 1 [W m^{-2}]
R''	Surface Reaction Rate [mol m^{-2} s^{-1}]
Re	Reynolds Number [-]
s	Cavity/Protrusion Spacing [m]
Sc	Schmidt Number [-]
Sh	Sherwood Number [-]
t	Plexiglass Cover Thickness [m]
T	Temperature [K]
u	Superficial Velocity [m s^{-1}]

Latin

$\mathbf{U}$	Velocity Vector [m s^{-1}]
V	Total Reactor Volume [m^3]
$\hat{V}^b$	Molar volume at the boiling point [cm^3 mol^{-1}]
W_R	Reactor Width [m]
y	Triangular Duct y-Coordinate [m]
z^*	Dimensionless Axial Length [-]
z	Triangular Duct z-Coordinate [m]

Greek Symbols

α	Film Absorptivity [-]
δ	Cavity/Protrusion Depth [m]
ε	Aspect Ratio [-]
κ	Extinction Coefficient [m^{-1}]
μ	Dynamic Visocisty [Pa s]
φ	Apex Half Angle [rad]
ρ	Density [kg m^{-3}]
σ	Spectral Distribution Standard Deviation[nm]
γ	Shape Parmeter [-]
λ	Wavelength [nm]

Subscripts

4CP	4-Chlorophenol
BA	Benzoic Acid
Bot	Bottom Relative to the Duct Apex Angle
Dst	Destination
i	Species
Max	Maximum depth
Min	Minimum Spacing Relative to the Top of the Duct
nd	Normal Diffuse
O2	Oxygen
Ref	Reference
S	Surface
Src	Source
W	Water
0	Initial
∞	Bulk liquid
λ	Spectral

Superscripts

T	Transpose
*	Transformed Parameter
’’	Surface

1 Introduction

1.1 Motivation

Amid rising environmental concerns due to increasing global population and rapid industrialization, the need for sustainable methods for energy production (e.g. H_2 production) and environmental remediation (e.g. CO_2 reduction and water treatment) has increased tremendously [1,2]. Regarding water pollution, harmful pollutants (e.g. 4-chlorophenol (4-CP)) are released into reservoirs through waste streams in a variety of industries, including dye production, pharmaceuticals, pulp and paper mills, and food manufacturing plants [3]. Consequently, the accumulation of persistent, non-biodegradable organic pollutants such as chlorophenols poses a major environmental hazard to both human and aquatic life, even in trace amounts, due to their resistance to degradation [4,5]. For example, the accumulation of dyes in open water systems can lower the ability of oxygen and solar radiation to reach organisms, leading to potential risks to life [6]. Moreover, heavy metals within discharge streams can bioaccumulate, leading to long-term environmental damage due to their persistent and toxic properties [5]. As such, the need for effective water treatment techniques to sustainably remove a large amount and variety of persistent compounds is increasingly evident.

1.2 Background

Conventional water treatment options such as sedimentation, filtration, reverse osmosis and activated carbon adsorption are reliable, industrially tested processes, but can suffer from high costs, difficulty with increased volume, and an inability to mineralize pollutants completely, rendering them unsustainable long-term [7,8]. To address these concerns, advanced oxidation processes (AOPs) have emerged as a promising alternative for water treatment. Specifically, AOPs using semiconductor-assisted photocatalysis are preferred primarily due to their utilization of the solar energy spectrum, making it a sustainable process with the ability to effectively degrade a variety of different organic compounds [9]. Applications such as solar water heating and passive disinfection are well posed for AOPs due to the large access to sunlight.

In AOPs, treatment is done by reacting undesired compounds (e.g. organic pollutants and water pathogens) with generated hydroxyl radicals (OH^-), which are highly reactive [10]. The result is complete mineralization through oxidation of the compounds, yielding less harmful end products. Semiconductor-assisted photocatalysis is the mechanism in which the hydroxyl radicals

are generated via illumination [9]. At a high level, a photocatalytic reaction contains three main steps. First, photons are absorbed from irradiation by the photocatalyst, which promotes an electron from its valence band to the conduction band, yielding a negatively charged radical and a positively charged hole. Next, these radicals can migrate to the photocatalyst surface, where they can then react in redox reactions. Finally, the generated radicals can recombine before reacting at the surface. Sufficient time is needed for the produced charge carriers to migrate to the surface before recombination to degrade incoming pollutants [11].

1.3 Current Limitations

Currently, photocatalytic technologies suffer from both catalytic inefficiencies as well as limited progress in the design and scale-up of industrially feasible photoreactors [12]. Catalytically, high recombination rates limit the surface reaction rates, whereas inefficient usage of visible light limits the sustainability of the process since the visible light portion only makes up 42-43% of the solar spectrum [13–15]. Recombination rates are highly dependent on the crystalline structure and particle size of the semiconductor [13]. A highly crystalline structure with few defects limits the number of recombination sites, and a smaller particle size minimizes the distance the charge carriers must migrate to reach the catalyst surface, thereby increasing the overall surface reaction rate [13].

On the design side, the photocatalytic rate and energy efficiency are limited in part by the insufficient ability to deliver photons to the catalyst surface [16,17]. Increasing the photon delivery requires design and analysis of surface and optical properties, as well as photoreactor geometry and illumination source. Therefore, when designing an industrially feasible photoreactor, the kinetic, hydrodynamic, and radiation effects must all be considered, since all the effects coupled together govern the energy efficiency of the reactor [18]. By combining experimental kinetic results with tools such as computational fluid dynamics (CFD) for solving the governing hydrodynamics and radiation transfer, detailed modelling of photoreactors which couple the effects of radiation transport as well as both volumetric and surface reactions is possible [1]. Furthermore, simulation tools allow for flexible parametric studies using various geometrical configurations.

1.4 Catalyst Deployment

The configuration of the catalyst in photoreactors has major effects on the performance of the photoreactor, the lifecycle of the catalyst, and the complexity of the process. The two most

common methods of catalyst deployment in photoreactors are through surface immobilization (e.g. thin film coatings) or by introducing the catalyst as a dispersed phase (e.g. slurry reactor). Early research on photoreactors used TiO_2 suspensions due to the high specific surface area of the catalyst pellets [19]. Unfortunately, using particle suspension has downsides, namely, downstream separation, difficulty using suspended photocatalysts in continuous processes, and particle aggregation and agglomeration at high concentration [19]. Agglomeration, caused by fine particle sizes and high surface energy, is highly detrimental to catalyst preservation and reusability, as well as lowering the specific surface area, causing reduced surface reaction rates [10]. Due to these concerns, immobilization is generally preferred since there is no need for particle separation. Other advantages include a highly porous catalyst layer, which can provide a high surface area, and the ability for conductive materials to be used as support to reduce electron-hole recombination through removal of excited electrons [20]. Disadvantages of immobilization include lower photon accessibility and increased external mass transfer effects [20]. While the immobilized configuration is simpler for industrial use, if the efficiency of the slurry configuration is high enough, it could overcome its drawbacks. Comparison between the two and techno-economic studies are required to truly decide which is better for industrial use. In this work, immobilization is used due to the advantages. One of the main goals is to address the disadvantages and attempt to improve them through analysis of the hydrodynamics and the geometrical configuration.

1.5 Photoreactor Geometry

The main impacts of photoreactor geometry are on the photoreactor hydrodynamics and the radiation transfer. Both these effects need to be optimized simultaneously to minimize the effects of mass transfer limitations and insufficient photon flux at the catalyst sites. Zhang et al. [16,17,21] used a corrugated plate reactor (CPR) and found a higher energy efficiency (37 kWh/m^3) and a 150% improvement in the reaction rate when compared to a flat plate reactor under the same conditions. This superior performance was attributed to a larger illuminated catalyst surface area and the ability for the corrugations to recapture reflected photons. It was also found that a smaller apex angle led to higher degradation rates due to higher mass transfer rates, even at the cost of less uniform radiation profiles. The main limitation of this geometry was its inability to illuminate the backside of the corrugations, leading to an inefficient flow distribution. To remedy this problem, Zhao et al. [14,15] modified the design by introducing slants to the corrugations, appropriately named a slant plate photoreactor (SPR). Through this modification, a higher energy

efficiency was observed, and a 12% improvement in the reaction rate was seen when compared to the CPR at the same angle. Zelic et al. [22] studied the effects of adding rotation to a cylindrical type photoreactor. They found increased mass transfer through this external mixing, and a slight increase over the flat plate reactor, but the comparison was not consistent due to differing numbers of lamps and total catalyst surface area. However, their study does highlight the strong dependence of the surface reaction rate. In another study, Qi et al. [18] used CFD to model an annular bubble column reactor. Using an annulus for the geometry does have the benefit of making the catalyst surface immobilization easier, but no comparison to any other reactor geometry was done. This study does show the benefits of using CFD as a tool to model multiphase transport using a specific geometry. Depending on geometry, there exist trade-offs between the coupled mass and radiation transfer in the reactor; as such, coupled modelling and optimization of geometric parameters are vital in any feasible photoreactor design.

1.6 Protrusion/Cavity Reactor

It is evident from photocatalytic literature that the reactor geometry has a large impact on both the mass transfer rates and the absorbed radiation fields, which both play a critical role in the degradation rate. Mass transfer is especially important when the radiation intensities are high (> 250 W m^{-2}) [23] or when the diffusivity of the pollutants is low (e.g. 4-chlorophenol) [21]. This limiting regime can be seen in both macro- and micro-scale photoreactors under low laminar flows [24] as well as within slurry reactors at high catalyst loadings [25]. As previously mentioned, even though immobilized systems have benefits over dispersed catalyst deployment, they are more susceptible to mass transfer limitations due to lower exposed surface area and the creation of a diffusion boundary layer in laminar flow. As such, there is a need to improve mass transfer while not compromising on the radiation field.

One method to increase mass transfer in laminar flows passively, which is popular in broader heat transfer literature, is through the addition of surface modifications, particularly through added roughness via baffles, cavities, or ribbed structures on the reactive surface. Previous studies, including those of Ligrani et al. [26] and Qu et al. [27] have shown an increase in heat transfer through the addition of hemispherical protrusions or cavities (also known as pimples and dimples) due to the added secondary flows and vortices created by the modifications. Both shallow and deep cavities were tested, and those with a diameter-to-depth ratio of 0.15 to 0.2 were found

to have the largest benefit due to the increase in recirculating flows within the dimple [27]. The choice of modification geometry is not limited to rounded shapes. In the study of Ebrahimi and Naranjani [28], they showed a similar type of enhancement using square pyramidal-shaped protrusions via cross-mixing.

This idea of surface modification can also be applied to photoreactors, with the closest direct precedent being the study of Rasul et al. [29]. In this study, both laminar and turbulent flows were tested using semi-circular, triangular, and rectangular surface baffles. Their results showed a minimum increase of 8% and a maximum of 37% in the mass transfer rates due to the increase in turbulence caused by the baffles and surface roughness. While hydrodynamics was well studied, this paper did not couple the radiation field into the results. Not examining the radiation field directly could vastly overestimate the increase in photoreactor performance, especially since baffles could suffer from self-shadowing.

Based on a survey of the photocatalytic literature, outside of this study, there is little research done on the combined modelling of surface-enhanced laminar flows that combine both hydrodynamic modelling and radiation modelling. As such, there is novelty in photocatalytic research in attempting to study those combined effects using surface modifications. Cavities and protrusions seem most promising since they have already been shown to be adept at increasing heat transfer. Furthermore, since photocatalytic pollutants generally have higher Schmidt numbers, they may be more susceptible to small heat transfer enhancements due to their thin diffusion boundary layers. However, it should be noted that they run the risk of receiving less light due to self-shadowing or having weakly exchanging fluid zones depending on the bulk flow profile.

1.7 4-CP Degradation Kinetics

Before modelling a photoreactor, kinetic data must be determined experimentally, so it can be used as a reaction source term. Most commonly, Langmuir-Hinshelwood (LH) models are used to describe degradation kinetics, but they are not always decoupled from external mass and radiation effects. Moreover, LH models alone do not fully describe the effects of photon absorption, charge carrier generation, recombination, and trapping [30]. However, these effects can be considered using an averaged approach by including terms such as catalyst concentration, intrinsic quantum yield, and the local volumetric rate of photon absorption [30].

In this work, degradation of 4-chlorophenol (4-CP) is used as a model pollutant due to its presence in wastewater steams and the availability of experimental degradation data from Zhang et al. [21]. There have been previous studies performed on the photodegradation of 4CP on TiO_2 films. In the study done by Mills and Wang [31], intrinsic kinetics of 4-chlorophenol degradation on TiO_2 films were obtained independent of mass transfer using a highly agitated bench-scale mixture at constant temperature and saturated with oxygen. Moreover, since the reaction film area in the apparatus is small, the photon delivery can be assumed to be incident, which allows for a simple calculation of the absorbed photon flux. In another study done by Satuf et al. [32], the degradation of 4CP using TiO_2 dispersions was done on a flat plate. This study explicitly modelled the radiative effects by computing the radiative transport equation using the discrete ordinates method and proposed a series of reaction rates estimating the production of reaction intermediates such as 4-chlorocatechol and hydroquinone. Additionally, a reduced-order model for the overall disappearance of the parent compound was developed. Modelling aspects and observed trends from both works lay the basis for some of the methodology presented in this work as well as justification in the results.

1.8 Research Goals

The goals of this work are twofold. First, a kinetic model describing the degradation kinetics, decoupling the effects of mass and photon transfer, must be obtained to use as a surface reaction term in the subsequent modelling. Experimental data taken from the studies done by Zhang [16,17,21] on flat plate photoreactors is used since the geometry is simple, the effect of Reynolds is captured experimentally, and the radiation properties are well defined. This work offers an advancement over the modelling done previously by Zhang in the determination of both mass transfer and radiation modelling. Mass transfer coefficients are compared to existing literature data, and the spatial radiation field is determined using Monte Carlo ray tracing. The new fitting also corrects a dimensional inconsistency in the rate expression of the previous work. Lastly, the effects on the experimental design considerations are discussed, and recommendations for future improvements are offered.

The second goal of this work is to utilize the intrinsic kinetics to investigate the performance of a surface-enhanced corrugated plate (SECP) photoreactor using both protrusions and cavities. Corrugated plate photoreactors have been previously studied and shown to increase

degradation performance through their higher mass transfer rates and larger photon recapture compared to other simple geometries such as the flat plate [21]. Furthermore, to the authors' knowledge, there has not been a study comparing the coupled mass transfer and radiation effects of cavities and protrusions fixed onto a triangular duct. A baseline case of the unmodified corrugated plate photoreactor is presented for comparison. Laminar flow is used for each geometry due to the large availability of literature data, making the computational methodology possible to validate in the absence of in-house experimental data. The effects of the radiation source are also presented. The benefit of this work for the future is to determine through simulation whether this design could improve the degradation rate through increased mass transfer while also not disrupting the radiation field.

All following sections are divided into subsections relevant to the kinetic estimation (KE) and to the SECP reactor, respectively. Chapter 2 outlines the model development including the experimental conditions and the computational models used to estimate the kinetic parameters and the novel SECP geometry. Chapter 3.1 presents the results of the kinetic fitting which accomplishes the first goal of this work. Chapter 3.2 presented the results of the investigation of the SECP in line with the second objective. Of note, any mention of cavities is used interchangeably with dimples. Likewise, any mention of protrusions is used interchangeably with pimples.

1.9 Novelty and Impact

Through accomplishment of the research goals this work provides a detailed workflow for estimating intrinsics kinetic parameters through explicit simulation of the flow field, species transport, and the absorbed radiation field. Furthermore, modelling of surface enhancements could lead to promising passive mass and radiation transfer improvement regardless of the macroscale geometry. This opens the door for a large addition of research to this field by analyzing different surface enhancements on existing or novel reactor geometries leading to improved performance of surface immobilized photoreactors.

2 Model Development

2.1 Experimental Conditions

2.1.1 Kinetic Estimation

The experimental data are time-evolved 4-CP concentration data from measurements made on a flat plate photoreactor immobilized with TiO_2. The flat plate photoreactor setup consists of a rectangular duct with flow entering a stainless-steel screen enclosure packed with 5 mm glass beads, which act as a flow redistributor. This setup attempts to make the flow more uniform at the duct inlet. The inlet stream consists of a dilute water mixture containing 4-CP with an initial concentration of 30 ppm and oxygen at its solubility limit of approximately 7 ppm [21]. The bottom portion of the reactor is coated with a TiO_2 (Degussa) film. The top of the reactor is covered with a thin piece of UVT acrylic Plexiglass. The average weight across the catalyst film is assumed constant at 1 mg TiO_2 cm^{-2} [17]. Three 40 W fluorescent UV lamps (Phillips, TLK 40W/10R) are stationed above the setup to allow diffuse light to travel through the semi-transparent cover. The output stream of the reactor is sent to a sampling vessel followed by a water bath to maintain the temperature at approximately 26.5°C. Afterwards, the cooled stream is recirculated back to the input. The total reactor volume is set at 3.8 L. A schematic of the reactor geometry is given in Figure 2.1.

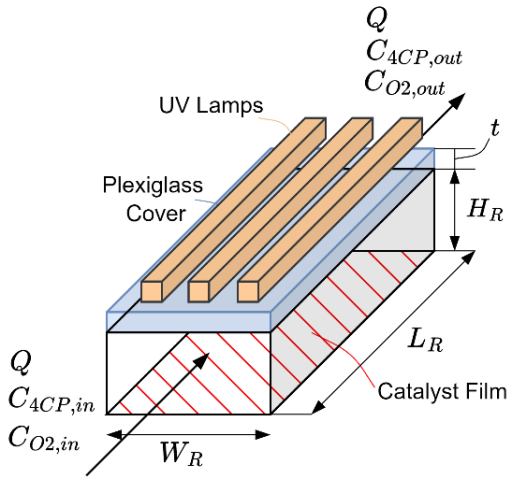


Figure 2.1. Isometric schematic of the flat plate photoreactor setup highlighting the lamp arrangement, acrylic cover, catalyst film, and flow direction.

The reactor dimensions consistent with Figure 2.1 are summarized in Table 2.1.

Table 2.1. Summary of reactor dimensions for the flat plate photoreactor

Dimension	Value [m]
Reactor Height, H_R	0.025
Reactor Width, W_R	0.080
Reactor Length, L_R	0.5
Cover Thickness, t	0.00635

The flow and radiation conditions tested experimentally by Zhang [21] are given in Table 2.2. Several Reynolds numbers and radiation intensities were tested using the flat plate case to see the effects of mass transfer and absorbed radiation on the reaction rate. Notably, the Reynolds number is defined by an arbitrary characteristic length scale, $\mathcal{L}$, via Equation 2.1. This arbitrary definition is used since the Reynolds number has context-dependent definitions. In the work of Zhang [21] the Reynolds number is based on hydraulic diameter; whereas, as will be discussed in Section 2.3, the mass transfer coefficients from literature are defined using the square root of the cross-sectional area for the length scale. Moreover, discussion pertaining to the packed bed flow distributor utilizes particle diameter as the length scale.

$$Re_{\mathcal{L}} = \frac{\rho u \mathcal{L}}{\mu} \tag{2.1}$$

Table 2.2. Flow and radiation conditions for the flat plate.

Geometry	Re_{dh}	u [m s^{-1}]	I [W m^{-2}]
Flat plate	431	0.009	122
	782	0.017	122
	1633	0.036	122
	4313	0.096	15,43,122
	5813	0.1301	122

[1]The Reynolds number is defined using hydraulic diameter (Equation 2.2) as the characteristic length scale.

$$d_h = \frac{4A_c}{P} \tag{2.2}$$

2.1.2 Surface-Enhanced Corrugated Plate

The surface enhancement of the corrugated plate is done by placing hemispherical cavities along the planar surface of the hypotenuse. The cavity imprints yield geometrically similar protrusions on the opposite side. This geometry is given visually by Figure 2.2. The overall reactor dimensions of the surface-modified corrugated plate follow the same conventions summarized in

Table 2.1. The unmodified corrugated plate reactor follows the same overall geometry as Figure 2.2 except for the surface modifications.

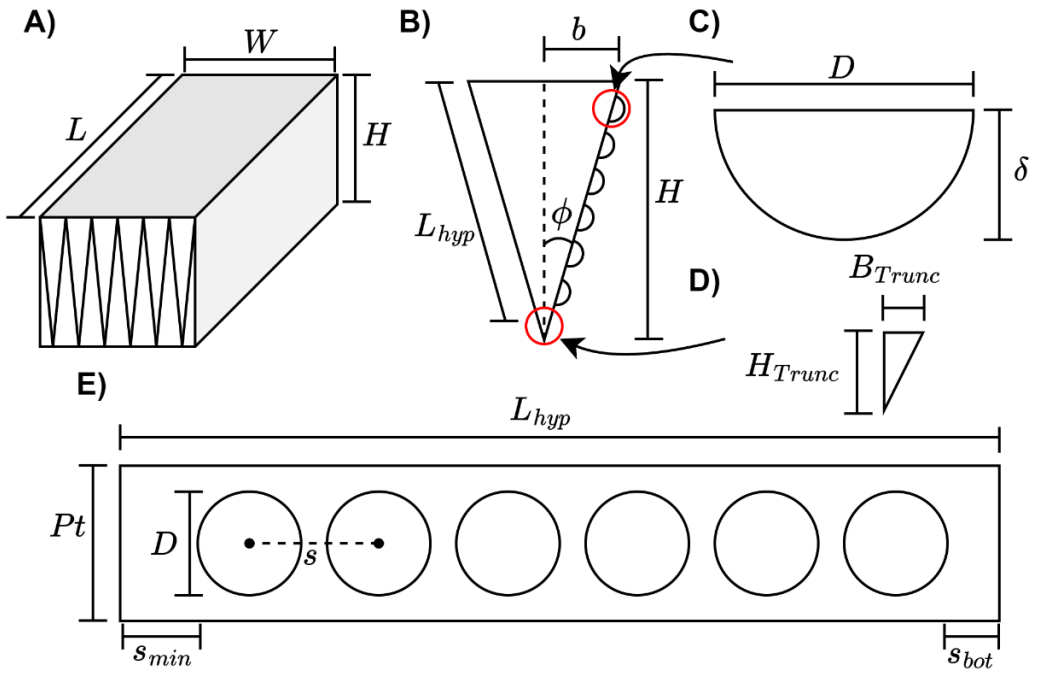


Figure 2.2. A) Overall schematic of the corrugated plate photoreactor consistent with the dimensions given in Table 2.1. B) Dimensions of the triangular duct that makes up each corrugation. C) Zoomed-in depiction of the hemispherical surface modifications. D) Zoomed-in depiction of the tip truncation for meshing purposes. E) Planar surface showing the alignment of the surface modifications on a unit cell.

The corrugated geometry is split into N_t number of triangular ducts by dividing the reactor width by the number of top ducts desired. Six channels were desired since it produces a small apex angle, which was found previously to increase the degradation rate due to higher mass transfer rates and a potentially more uniform radiation profile due to increased reflections [17,33]. The half base of each triangular duct is given by Equation 2.3.

$$b = \frac{W}{2N_t} \tag{2.3}$$

The half apex angle is then given by simple trigonometry (Equation 2.4).

$$\phi = \text{atan}\left(\frac{b}{H}\right) \tag{2.4}$$

The tip of the triangular duct is truncated by a height of 1 mm (H_{trunc}) for the purposes of creating a structured quadrilateral mesh; the reasoning is explained in the Appendix. The truncated base and hypotenuse are given by Equations 2.5 and 2.6.

$$b_{Trunc} = \tan(\phi) H_{Trunc} \tag{2.5}$$

$$L_{hyp} = \frac{(H - H_{Trunc})}{\cos(\phi)} \tag{2.6}$$

Three main dimensions can be used to specify the geometry of the surface features: the number of unit cells, the ratio of pitch to diameter, and the ratio of diameter to height. The number of unit cells controls how many dimples fit into the duct length. This parameter also defines the pitch (length of a unit cell), which is equivalent to the diameter of the dimple added to half the spacing on each side, creating a repeating cell (Equation 2.7).

$$Pt = \frac{N_u}{L} = d + s \tag{2.7}$$

The pitch-to-diameter ratio controls the center-to-center spacing. A larger ratio spreads the dimples further apart, while a smaller ratio packs them densely. To avoid overlap, Equation 2.8 gives the necessary condition.

$$\frac{Pt}{D} \geq 1 \tag{2.8}$$

The depth-to-diameter ratio controls the depth of the dimple relative to its diameter. A higher ratio produces deeper dimples; a smaller ratio produces shallower dimples. Once these parameters are defined, the rest of the array geometry can be fully specified through Equations 2.9 and 2.10.

$$D = \left(\frac{Pt}{D}\right)\left(\frac{1}{Pt}\right) \tag{2.9}$$

$$s = Pt - D \tag{2.10}$$

Due to the small apex angle present in the corrugated plate, it puts some restriction on how large the dimples can be. If the dimples are too large, their imprints will collide with one another on the opposite side of the plate. Thus, a minimum clearance height was calculated assuming the value of depth-to-diameter to be studied is 0.2 (Equation 2.11). Furthermore, a 50% clearance factor was also used. This value is then computed by Equation 2.12.

$$\delta_{max} = 0.2D \tag{2.11}$$

$$s_{min} = 1.5\left(\frac{\delta_{max}}{tan\phi} - \frac{D}{2}\right) \tag{2.12}$$

The bottom spacing of the last dimple is computed as the residual of the number of cavities, the diameter, the spacing and the minimum top spacing via Equation 2.13.

$$s_{bot} = L_{hyp} - N_D D - (N-1)s - s_{min} \tag{2.13}$$

The bottom spacing is minimized to allow for the largest number of dimples on the planar face by computing Equation 2.14. N must be an integer number of cavities, so the floor is taken.

$$N_D = \left\lfloor \frac{\left(L_{hyp} + s - s_{min}\right)}{Pt} \right\rfloor \tag{2.14}$$

The dimensions of the surface modifications are presented in Table 2.3.

Table 2.3. Summary of surface modification dimensions

Dimension	**Value [m]**
Pitch to Diameter Ratio, Pt/D	1.5
Depth to Diameter Ratio, δ/D	0.20
Number of Unit Cells, N_u	100
Number of Triangular Ducts, N_t	6

The depth-to-diameter ratio of 0.20 was selected as a baseline case since it is regarded as a moderate cavity depth that exhibits dynamic vortical flow structures which could enhance mass transfer for low-diffusivity liquids [26,27]. The pitch to diameter and number of unit cells were chosen somewhat arbitrarily as a baseline case. The main goal of this study is to examine any potential benefits or drawbacks that the cavities and protrusions have on the flow structures and radiation field. This baseline case could then motivate and guide future work in optimizing the geometry to maximize any flow benefits without disrupting the radiation field.

The range of flow conditions tested is summarized in Table 2.4. Notably, the pressure drop is listed as well as the resulting inlet velocity and Reynolds number since the periodic unit cell used specified pressure drops to drive the flow. Furthermore, for the species transport, the same inflow values of 4CP (30 ppm) and oxygen (7 ppm) are used.

Table 2.4. Summary of flow conditions tested for the SECP reactor.

Geometry	**ΔP [Pa]**	**u [m s^{-1}]**	**Re_{dh}**
SECP	0.01, 0.05, 0.1	0.011, 0.054, 0.100	182, 904, 1796

2.2 Kinetic Model

The following kinetic model is shared across both the kinetic estimation and the SECP plus baseline reactor geometries. The complete photo-oxidative mineralization of 4-CP using TiO_2 as the catalyst is given by Equation 2.15 [21,31].

$$2\ ClC_6H_4OH + 13\ O_2 \xrightarrow{h\nu \geq 3.2eV} 12\ CO_2 + 4\ H_2O + 2\ HCl \tag{2.15}$$

Previous work [21,31] has shown that the photodegradation of 4-CP produces several organic reaction intermediates such as 4-chlorocatechol and hydroquinone, along its reaction pathway to complete mineralization. However, in this system, it was determined by Zhang [21] using high-performance liquid chromatography that the reaction intermediates are produced in low enough quantities, rendering them kinetically negligible over the long degradation period. As a result, the degradation of 4-CP is sufficiently modelled assuming full mineralization.

The bulk mass balance of 4-CP through the recirculation reactor is modelled as a simplified batch reactor. This is justified since the degradation of the parent compound is kinetically slow, which results in a very low single-pass conversion. The temporal evolution of the bulk concentration is then only a function of its surface reaction rate and the amount of total liquid volume present in the system. This is represented by the global ordinary differential equation given by Equation 2.16. Notably, the weight of the catalyst film is assumed constant with a uniform coating, so catalyst loading is not considered directly.

$$\frac{dC_b}{dt} = -\frac{1}{V}\iint_S r''_{4CP}\,dS \tag{2.16}$$

A standard LH model accounting for light dependency as well as adsorption of 4-CP and O_2 is proposed as a suitable model for this system (Equation 2.17).

$$r''_{4CP} = \frac{k_0 K_1 K_2 C_s O_s}{(1 + K_1 C_s)(1 + K_2 O_s)}\left(\frac{q}{q_{ref}}\right)^n \tag{2.17}$$

Where q_{ref} is simply a reference value of 1 W m^{-2} to keep the equation dimensionally consistent.

Photoactivation dependences, such as hydroxyl generation and electron-hole recombination rates, are lumped into a single parameter called the local area-specific rate of energy absorption (LASREA), q, which varies with the light dependency parameter, n. LASREA is the total amount

of radiative energy absorbed by the catalyst material on its surface. Since the film surface is under constant illumination from lamps with a fixed position, and there are no particulates in the solution to create scattering, the spatial distribution of the LASREA is considered constant for each geometry. The radiation model to compute this quantity is outlined in Section 2.4.

The surface concentrations of 4-CP and O_2 are a direct function of reactant supply via normal diffusion into the catalyst surface and the consumption due to the surface reaction. This coupled flux balance is given by Equations 2.18 and 2.19.

$$k_{4CP}(C_b - C_s) = r''_{4CP} \tag{2.18}$$

$$k_{O_2}(O - O_s) = r''_{O_2} \tag{2.19}$$

The surface reaction rate of oxygen is related to the rate of 4-CP consumption through the stoichiometry in Equation 2.15. Accordingly, the relative rates are given by Equation 2.20.

$$\frac{r''_{4CP}}{-2} = \frac{r''_{O_2}}{-13} \tag{2.20}$$

Once the mass transfer coefficients and the LASREA are known, the bulk mass balance (Equation 2.16) can be solved by computing the system of coupled surface concentrations, followed by integrating the surface reaction rate and then stepping in time. The intrinsic kinetic parameters, k_0, K_1, and K_2, are estimated through nonlinear regression. Finally, once the kinetic parameters are known, they can be used directly to model the performance of the SECP and the baseline case.

2.3 Convective Mass Transfer

2.3.1 Kinetic Estimation

As presented in Table 2.2, in this system the Reynolds number varies from 431 to 4313. Mass transfer coefficient data are presented both from reported literature and measured by Zhang [21]. For internal pipe flows, laminar conditions are present at Reynolds numbers less than 2000-2300 (depending on duct smoothness) and transitional to turbulent flow at higher Reynolds numbers [34,35]. Extensive work has already been done both experimentally and numerically to estimate the laminar flow profiles and thermal/mass transport in simple geometries such as rectangular, triangular, and circular ducts. A summary of these correlations is presented in the work of Shah and London [35]. Since there is a non-circular duct shape used in this work, the model of Muzychka and Yovanovich [36] (which is validated using the results of Shah and London [35])

limits the effects of the duct geometry through their model by using the square root of the cross-sectional area as the characteristic length. Using this model, the convective mass transfer coefficients for laminar flow ($10 \leq Re_{\sqrt{A}} \leq 100$) are computed from Equations 2.21-2.23.

$$fRe_{\sqrt{A}} = \frac{12}{\sqrt{\epsilon}(1+\epsilon)\left[1 - \frac{192\epsilon}{\pi^5}\tanh\left(\frac{\pi}{2\epsilon}\right)\right]} \tag{2.21}$$

$$z^* = \frac{L}{\sqrt{A}Re_{\sqrt{A}}Sc} \tag{2.22}$$

$$Sh_{\sqrt{A}}(z^*) = \left[\left\{0.6135\left(\frac{fRe_{\sqrt{A}}}{z^*}\right)^{\frac{1}{3}}\right\}^5 + \left\{3.24\left(\frac{fRe_{\sqrt{A}}}{8\sqrt{\pi}\epsilon^{\gamma}}\right)^5\right\}\right]^{1/5} \tag{2.23}$$

Where the dimensionless length, z*, uses the full reactor length, L. The shape parameter $\gamma$is 1/10 for the flat plate and -1/3 for an isosceles triangular duct. This serves as the lower bound for the mass transfer coefficient. It will be shown in the following sections that the Reynolds dependency on the kinetic data does not follow the theoretical mass transfer scaling (for Reynolds numbers less than 2000) as presented in the above equations due to the presence of the flow distributor.

To evaluate the mass transfer coefficients from the literature data presented in Equations 2.21-2.23, the required fluid properties are the mixture density, viscosity, and mass diffusivity of 4-CP. Since the solution is considered dilute (30 ppm), it is assumed that any reduction in species concentration does not change the mixture properties appreciably. Furthermore, any temperature dependency on the properties is neglected since the fluid temperature is assumed to be relatively constant throughout the recirculation reactor. Water density and viscosity are estimated from IAPWS data [37,38]. The mass diffusivity of 4-CP was calculated via the Wilke-Chang correlation (Equation 2.24) [39] using an association parameter of 1.61, which agrees well with the molecular simulation results of Martins et al. [40].

$$D_{4CP,W} = \frac{7.4 \cdot 10^{-8}\left(\phi \widehat{M}_W\right)^{0.5} T}{\mu_W \left(\widehat{V}_{4CP}^{b}\right)^{0.6}} \tag{2.24}$$

The mass diffusivity of oxygen was computed from the CRC handbook. A summary of the properties of the fluid mixture is given in Table 2.5.

Table 2.5. Summary of the inlet stream properties at 26.5°C.

Species	Property				References
	Density [kg m^{-3}]	Viscosity [mPa s]	Diffusivity in Water [m^2 s^{-1}]	Molecular Weight [g mol^{-1}]	
Water	996.6	0.850	-	18.015	[37,38,41]
O_2	1.283	0.207	2.42E-9	31.99	[41]
4-CP	1.310	4.99	7.90E-10	128.55	[40,41]

Lastly, the average mass transfer data from the experiments conducted by Zhang [33] was collected using the benzoic acid (BA) dissolution method. A polynomial fit (Equation 2.25) was used to predict the average mass transfer coefficient over the flat plate.

$$\bar{k}_{BA} = 1.01 \cdot 10^{-4}\left[0.034\left(\frac{Re}{3273}\right)^3 - 0.145\left(\frac{Re}{3273}\right)^2 + 0.222\left(\frac{Re}{3273}\right)\right] \tag{2.25}$$

Assuming the near-wall boundary layer scaling, the dependence on the Schmidt number varies to the power of 1/3 [35,36] which in turn means the conversion of mass transfer coefficients from BA to 4-CP is done using Equation 2.26.

$$\bar{k}_{4CP} = \bar{k}_{BA}\left(\frac{D_{4CP}}{D_{BA}}\right)^{2/3} \tag{2.26}$$

The diffusivity of BA is reported as 1E-09 m^2 s^{-1} by Zhang [21].

2.3.2 Surface-Enhanced Corrugated Plate

To obtain estimates for the flow and mass transfer in the more complex SECP geometry, CFD was used to solve the governing transport equations. The convective flow field for an isothermal single-phase steady laminar flow is computed by solving the incompressible mass and momentum balances (Equations 2.27 and 2.28) [42].

$$\rho\nabla \cdot \mathbf{u} = 0 \tag{2.27}$$

$$\rho(\mathbf{u} \cdot \nabla)\mathbf{u} = \nabla \cdot [-p\mathbf{I} + \mu(\nabla\mathbf{u} + (\nabla\mathbf{u})^T)] \tag{2.28}$$

Fully developed flow is obtained by prescribing axial periodicity for the flow across one geometrically repeating section of the reactor called a unit cell. This assumes that the fully developed flow structure repeats itself from one unit cell to the next. To achieve this mathematically, the destination (outlet) velocity is mapped back to the source (inlet). The pressure

follows a similar mapping with the added inclusion of a set pressure drop, which drives the flow over the unit cell. These conditions are given mathematically by Equations 2.29 and 2.30.

$$u_{src} = u_{dst} \tag{2.29}$$

$$P_{src} = P_{dst} + \Delta P \tag{2.30}$$

To avoid a singular solution, the reference pressure must be set in the domain. Since the axial periodic conditions only set the pressure gradient, a pressure constraint is used directly on a single vertex in the domain, which is enough to constrain the problem for an incompressible flow.

At the centerline of the duct, symmetry conditions are applied. This is justified since the duct geometry is physically mirrored, identical boundary conditions are used on both sides of the mirror plane, and laminar flow does not exhibit fluid crossing the mirror plane. Equations 2.31-2.33 enforce no penetration and no shear stress across the mirror plane. On all other walls, the no-slip condition is enforced.

$$\mathbf{u} \cdot \mathbf{n} = 0 \tag{2.31}$$

$$\mathbf{K} = \mu(\nabla \mathbf{u} + (\nabla \mathbf{u})^T)\mathbf{n} \tag{2.32}$$

$$\mathbf{K} - (\mathbf{K} \cdot \mathbf{n})\mathbf{n} = 0 \tag{2.33}$$

Where **K** is the viscous stress tensor [Pa].

The above set of equations is enough to fully constrain the problem to solve for the fully developed flow profiles. Where possible, analytical solutions and published data are used to validate the numerical results for the convective field. All data were obtained from the source book written by Shah and London [35]. The fully developed velocity profile and friction factor for the triangular duct is calculated by Equations 2.34-2.36 using the geometrical conventions of Figure 2.3.

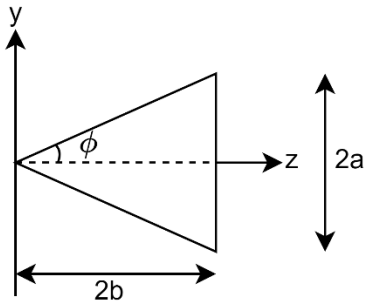


Figure 2.3. Geometric conventions for use in computing the fully developed velocity profile for an isosceles triangular duct.

$$u = -\frac{\Delta P}{2\mu L}\frac{y^2 - z^2\tan^2\phi}{1-\tan^2\phi}\left[\left(\frac{z}{2b}\right)^{B-2} - 1\right] \tag{2.34}$$

$$B = \left[4 + \frac{5}{2}\left(\frac{1}{\tan^2\phi} - 1\right)\right]^{\frac{1}{2}} \tag{2.35}$$

$$fRe = \frac{12(B+2)(1-\tan^2(\phi))}{(B-2)\left[\tan\phi + (1+\tan^2(\phi))^{\frac{1}{2}}\right]^2} \tag{2.36}$$

The pressure drop can then be computed from the definition of the Fanning friction factor (Equation 2.37).

$$\Delta P = \frac{2f\rho\bar{u}^2 L}{d_h} \tag{2.37}$$

Once the flow field is known, the species transport can then be computed. Recalling the assumption that the consumption of species does not significantly change the bulk flow properties, the flow field can be frozen, and species transport can be computed assuming one-way coupling. The transport of dissolved 4-CP and O2 is governed by the following steady-state convection-diffusion equation (Equation 2.38).

$$\nabla \cdot \mathbf{J_i} + \mathbf{u} \cdot \nabla C_i = R_i \tag{2.38}$$

Since the concentration of the species is low, the mass diffusion flux vector can be approximated using Fick's law of diffusion (Equation 2.39).

$$\mathbf{J_i} = -D_i \nabla C_i \tag{2.39}$$

To track mass transfer into the catalyst film, the normal diffusive flux is computed at the planar surface. This is given by Equation 2.40.

$$J_{nd,i} = \mathbf{J_i} \cdot \mathbf{n} \tag{2.40}$$

The normal diffusive mass flux is related to the concentration driving force through the local convective mass transfer coefficient.

$$J_{nd,i} = k_c(C_s - C_\infty) \tag{2.41}$$

To isolate the effects of mass transfer, an instantaneous reaction rate is prescribed at the reacting film surface. This is done by setting the surface concentration to zero everywhere on the film. As a result, the local convective mass transfer coefficient can be computed by Equation 2.42.

$$k_c = \frac{J_{nd,i}}{-C_\infty} \tag{2.42}$$

For comparison across the entire length of the reactor, the average mass transfer coefficient is computed by taking the surface area-weighted average of the normal diffusive flux via Equation 2.43. The average coefficient then follows the same general definition as Equation 2.42.

$$\bar{J}_{nd,i} = \frac{1}{A}\int_{\mathrm{A}} \bar{J}_{nd,i} dA = \bar{k}(C_s - C_\infty) \tag{2.43}$$

For non-reactive walls and the symmetry plane, the no-flux boundary condition is prescribed by Equation 2.44.

$$-\mathbf{n} \cdot (-D\nabla C) = 0 \tag{2.44}$$

The inflow is given by a flux (Danckwerts) condition (Equation 2.45). This is more numerically appropriate than a fixed inlet concentration since the film surface boundary is an instant mass sink. A fixed inlet concentration conflicts with the film Dirichlet condition and results in numerical oscillation at the corner cell vertices [42].

$$\mathbf{n} \cdot (\mathbf{J}_i + \mathbf{u}c_i) = \mathbf{n} \cdot \left(\mathbf{u}C_{i,0}\right) \tag{2.45}$$

Where $C_{i,0}$ is the specified upstream concentration [mol m^{-3}].

The species transported out of the domain is dominated by advection, and thus the outflow condition neglects diffusive transport, resulting in Equation 2.46.

$$\mathbf{n} \cdot (-D\nabla c) = 0 \tag{2.46}$$

Bulk concentration is defined as the far-field concentration, which is defined via a velocity-weighted concentration called the cup concentration (Equation 2.47). This represents the concentration of a perfectly mixed fluid through a cross section.

$$c_\infty = \frac{\int_A c(\mathbf{u} \cdot \mathbf{n}) dA}{\int_A (\mathbf{u} \cdot \mathbf{n}) dA} \tag{2.47}$$

Unlike the fluid flow, the species concentration across a unit cell is not axially periodic since the bulk concentration decreases as it is consumed at the reactive film. Thus, to model the entire length of repeated unit cells, the concentration at the outlet after reacting was mapped back to the inlet using Equation 2.48.

$$c_{src} = c_{dst} \tag{2.48}$$

The bulk concentration was then tracked explicitly through a time dependent ordinary differential equation. The ratio of viscous diffusion to mass diffusion is given by the dimensionless Schmidt number defined by Equation 2.49.

$$Sc = \frac{\mu}{\rho D} \tag{2.49}$$

Similarly, the ratio of convective mass transport to diffusive mass transport is given by the dimensionless Sherwood number for an arbitrary length scale, $\mathcal{L}$ defined by Equation 2.50.

$$Sh_{\mathcal{L}} = \frac{k\mathcal{L}}{D} \tag{2.50}$$

Since the Schmidt number is high, the viscous diffusion rate is much higher than the mass diffusion rate. This means the convective boundary layer thickens much faster compared to the diffusion boundary layer. Consequently, the combined entry length problem can be simplified to a Graetz flow problem, which uses the fully developed flow fields and computes the development of the mass diffusion boundary layer. This reduces computational cost since it removes the need for axial refinement when computing the convective flow field. Finally, the average mass transfer coefficients under Graetz flow for the comparison geometries are benchmarked against the Sherwood number predictions for a uniform boundary condition (within plus or minus 10%) of Muzychka and Yovanovich [36] via Equations 2.21-2.23. The results for the comparison case are validated using known solutions to the laminar flow, which can also be extended to the bulk flow

of the SECP since it does not change much with the surface modifications. Finally, a summary of the boundary conditions for the flow and species transport, with an accompanying schematic for visualization are given by Figure 2.4 and Table 2.6 respectively.

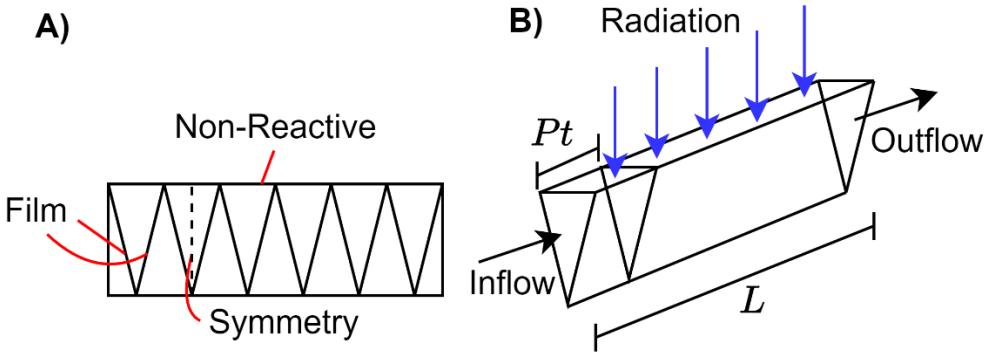


Figure 2.4. Schematic for visualization of the boundary conditions for the base case and SECP reactor.

Table 2.6. Summary of boundary conditions for the base case and SECP reactor.

Boundary	Flow Condition	Species Condition
Film	No-slip	Instantaneous consumption or Finite Surface Reaction
Non-reactive walls	No-slip	No flux
Symmetry	Symmetry/Mirror Plane	No flux
Inflow	Axial periodicity (destination)	Flux (Danckwerts) inflow
Outflow	Axial periodicity (source)	Outfall

2.4 Radiation Model

2.4.1 Kinetic Estimation

Following Figure 2.1, the light travelling from the lamps in the air to the plexiglass cover is modelled diffusely. Based on the manufacturer data for the Phillips TLK 40W/10R fluorescent lamps used, the spectral irradiance is given by a normal distribution fit by Zhang [21]. The lamp data and the unnormalized Gaussian are given in Figure 2.5. The spectral irradiance is normalized by the total irradiance, I, using Equation 2.51.

$$I_\lambda = \frac{I}{\sqrt{2\pi}\sigma} \cdot \exp\left(-\frac{(\lambda-\bar{\lambda})^2}{2\sigma^2}\right) \tag{2.51}$$

Where the standard deviation, σ = 15.75 nm is centered around $\bar{\lambda}$ = 353 nm.

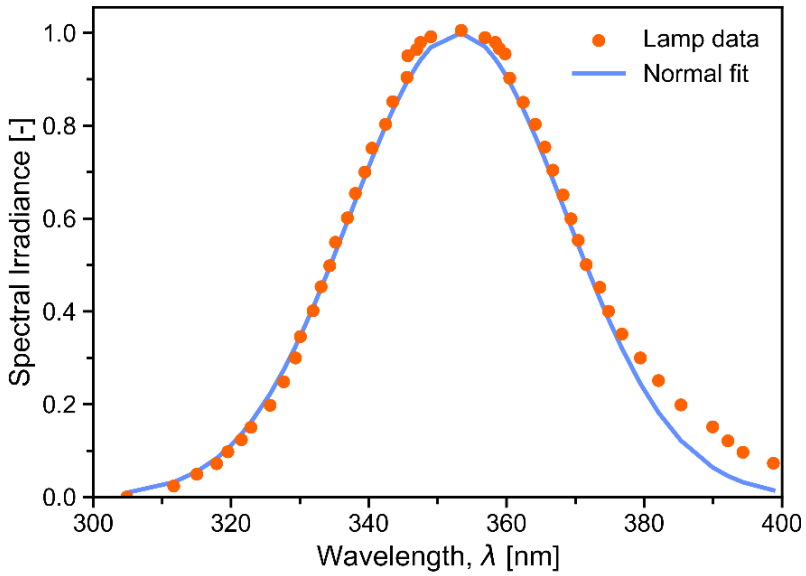


Figure 2.5. Spectral irradiance normal distribution produced by Zhang [21] based on the manufacturer data for the UV lamps

Once the light reaches the plexiglass cover, there is a material discontinuity resulting in refraction and reflection computed by the Fresnel equations [42]. The light then continues to travel through the cover and experiences refraction and attenuation due to absorption via the plexiglass medium. The refractive index for the plexiglass is assumed constant at 1.49 [33]. The extinction coefficient for the UVT acrylic cover is plotted in Figure 2.6 [33].

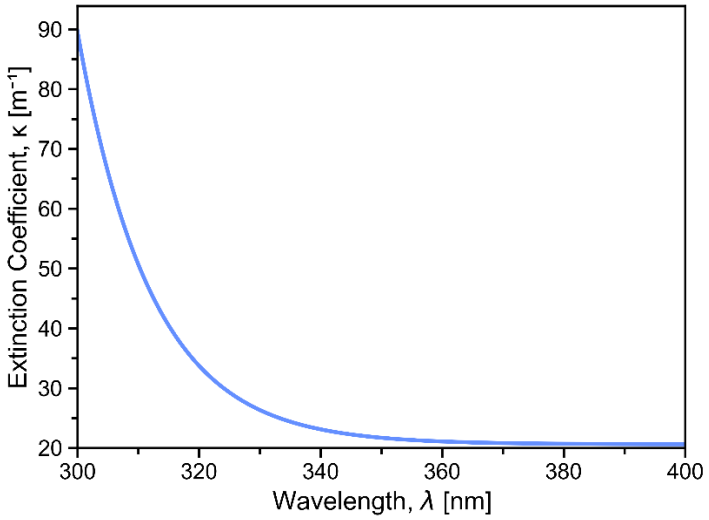


Figure 2.6. Spectral extinction coefficient of the UVT acrylic cover computed by Zhang [33]

Once the light reaches the end of the cover, there is another material discontinuity between the plexiglass and the water; this is again resolved by the Fresnel equations [42]. In the water domain, there is negligible scattering since there are no particulates, and the attenuation due to absorption is negligible. The refractive index is also assumed constant at 1.34, which is valid for this spectral range [43]. Once the light reaches the film surface, it undergoes spectral absorption. Any reflected light is diffuse, assuming the catalyst film is rough [33]. The data for the spectral absorption coefficient for the TiO2 film is plotted in Figure 2.7.

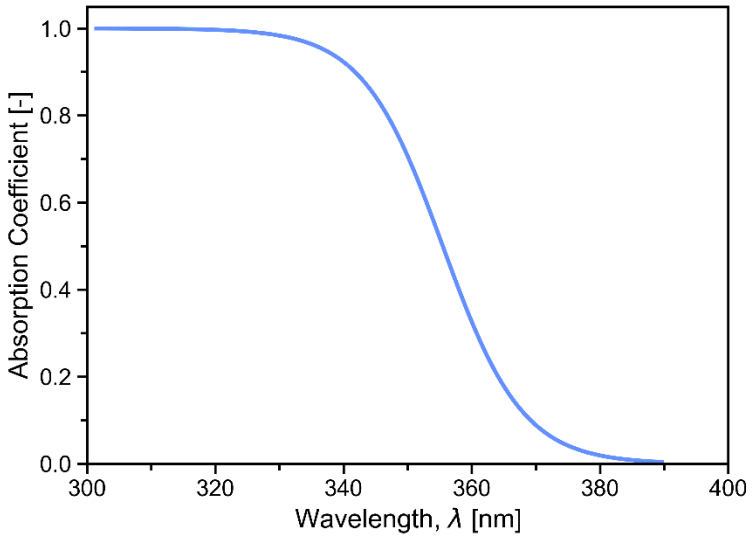


Figure 2.7. Spectral absorption coefficient of the TiO2 film from Zhang [33]

Based on the data of Figure 2.6 and Figure 2.7, an exponential decay function and a sigmoidal function given by Equations 2.52 and 2.53 were fit for the extinction and absorption coefficients, respectively.

$$\kappa = 90.12 \cdot Exp\big(-0.08241 \cdot (\lambda - 296.76)\big) + 20.6043 \tag{2.52}$$

$$\alpha = \frac{1}{\Big(1 + Exp\big(0.1604(\lambda - 355.47)\big)\Big)} \tag{2.53}$$

To ensure memory efficiency in the CFD solver, all spectrally dependent properties are divided into 9 discrete band ranges to fully capture the light distribution. The calculation of each property was done using a weighted average based on the energy distribution given by Figure 2.5. This weighted average for the extinction coefficient (analogous for the absorption coefficient) is given by Equation 2.54.

$$\bar{\kappa} = \frac{\sum_i I(\lambda_i)\kappa(\lambda_i)}{\sum_i I(\lambda_i)} \tag{2.54}$$

Notably, the division of each band range was done non-uniformly. Higher-resolution band ranges were taken where the energy distribution is high and to capture the shape of the property curves. Lower-resolution ranges were adequate at the ends of the normal distribution since the fraction of light is low. Table 2.7 summarizes the calculated spectral properties and total irradiance for each band.

Table 2.7. Film absorptivity, acrylic extinction coefficient, and irradiance for each discrete spectral band.

Band	**λ_{min} [nm]**	**λ_{max} [nm]**	**α [-]**	**κ [m^{-1}]**	**I [W m^{-2}]**
1	300	320	0.998	42.38	2.12
2	320	335	0.982	27.01	13.01
3	335	345	0.911	23.08	21.50
4	345	350	0.778	21.95	14.24
5	350	355	0.615	21.49	15.12
6	355	360	0.422	21.19	14.53
7	360	365	0.249	20.99	12.63
8	365	375	0.103	20.82	17.01
9	375	400	0.012	20.69	9.57

Finally, once the radiation field is known at the film boundary, the LASREA can be computed by summing the spectral irradiance multiplied by its spectral absorption over all the wavelength bands. This is given by Equation 2.55.

$$q(x,z) = \sum_k \alpha_{\lambda_k} E_{\lambda_k} \tag{2.55}$$

A summary of the boundary conditions for the flat plate case is found in Table 2.8 using the conventions of Figure 2.8.

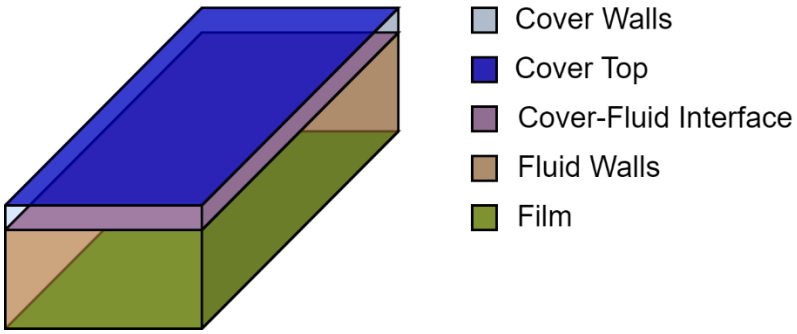


Figure 2.8. Schematic outlining the radiation boundaries.

Table 2.8. Summary of radiative boundary conditions for the flat plate.

Boundary	Ray Condition	Fluid Interface
Cover Walls	Transparent	Air-Plexiglass
Cover Top	Lambertian or Normal Rays	Air-Plexiglass
Fluid Walls	Transparent	Air-Water
Film	Diffuse Scattering	-
Cover-Fluid Interface	Transparent	Plexiglass-Water

2.4.2 SECP

The radiation model for the SECP photoreactor and the accompanying baseline cases differ from the kinetic estimation case. To save computational time, only the monochromatic radiation field of a single wavelength was tracked without the influence of the cover. This is a suitable simplification for a direct comparison study which attempts to isolate the geometrical influence. The wavelength chosen is 353 nm as it represents a large portion of the spectral distribution of the lamps, and its film absorptivity is approximately 0.6, meaning the effect of reflections is still captured by each geometry. In contrast to the KE model, the input radiation is modelled as either diffuse radiation or as collimated parallel rays to study the effects of the input radiation model. Modelling collimated parallel rays normal to the input surface is analogous to modelling direct overhead sunlight on a clear day.

For the baseline case, the entire reactor length is modelled since it does not take much computational effort. However, for the SECP reactor, only the unit cell is modelled; thus, the radiation is also only applied to this unit cell to save computational time. This assumption is effectively the minimum radiation the unit cell will receive since more of the diffuse reflections are not captured. In the future, a full-length model would be more accurate. The radiation boundary

conditions are given in Table 2.9 and follow the same schematic as Figure 2.4. Notably, the same intensity range used in the KE model is reused in the SECP model.

Table 2.9. Summary of radiative boundary conditions for the SECP and base case.

Boundary	Condition	Fluid Interface
Film	Diffuse Scattering	-
Non-reactive Top Wall	Lambertian or Normal Rays	Air-Water
Inflow & Outflow	Transparent	Air-Water

2.5 Computational Methods

2.5.1 Kinetic Estimation

COMSOL Multiphysics 6.4.0.293 was used to solve all the model equations due to its fast runtime, ease of use, and wide range of visualization tools built directly into the software. The radiation model was solved using Monte Carlo ray tracing via the geometrical optics interface. Spectral properties were input as either analytical functions or interpolation functions. The refractive index of the non-meshed domain was set to that of air (n = 1). The domain was discretized using a structured mesh to allow for convenient post-processing of the film spatial profile. To capture the full spectral range, a parametric sweep of monochromatic wavelengths was done using the wavelength bins outlined in Table 2.7. For all ray tracing cases, the input power is set to a reference value of 1 W. This allows convenient scaling for varying input intensities. The reference intensity is computed by multiplying the reference power by the area open to radiation, which is geometry dependent. For example, in the SECP, the area open to radiation was the top area of the unit cell. The proper scaling is then computed by multiplying the reference LASREA by the ratio of the reference intensity and the desired intensity via Equation 2.56.

$$q = q_{ref}\left(\frac{I}{I_{ref}}\right) \tag{2.56}$$

Deposited power was tracked on the film boundaries to estimate the LASREA for each spectral run. A balance of mesh resolution coupled with ray sampling was considered. Using a very coarse mesh smears the gradients in the spatial profile, whereas too few rays result in unphysical spatial profiles in the form of banding on the film surface. The deposited power profile was used as a convergence metric. In the kinetic model, the input radiation is modelled entirely diffusely, so the model used a combination of initial ray positions and angular ray directions to accurately estimate the diffuse source. Since the film has a large range of absorptivity, 100 000 secondary rays were

allowed in the system to track film reflections. Any rays exiting the domain through reflection were terminated. All side walls were assumed to be transparent. The time step specification for the solver was set to 15 ns. This is suitably long enough to ensure only the final steady solution is stored in the solver memory.

The global ODEs and DAEs interface was used to solve the bulk concentration and the surface flux balances. The default implicit adaptive BDF solver was used to solve the time-dependent ODEs. The spatial distribution for the radiation field was accessible to the solver through interpolation on a structured mesh using the coordinates of the film surface. Kinetic parameter estimation was done using COMSOL's dedicated parameter estimation interface due to its ability to handle datasets with varying experimental parameters, namely Reynolds number and radiation intensity. The Levenberg-Marquardt algorithm was used since it provides an efficient approach for parameter estimation, making use of the robustness of gradient descent combined with the rapid convergence of Gauss-Newton with good initial guesses [44]. The surface reaction rate is given to the optimizer algorithm in the algebraically equivalent form of Equation 2.57. This form allows for better numerical conditioning since the kinetic parameters now have a comparable scale to the surface concentrations, which can improve convergence for gradient-based optimizers [45]. Sensitivity to the parameters were also tested.

$$r''_{4CP} = \frac{k_0 C_s O_s}{(K_1^* + C_s)(K_2^* + O_s)} \left(\frac{q}{q_0}\right)^n \tag{2.57}$$

Where the adsorption coefficients, K^*, are in reciprocal form. Lastly, to enforce positive kinetic parameters, they are given to the estimator as logarithmic parameters in the form of Equation 2.58.

$$k_0 = 10^{logk_0} \tag{2.58}$$

2.5.2 Surface-Enhanced Corrugated Plate

The flow field was computed using the laminar flow interface (SPF). Taylor-Hood elements (P2+P1 discretization) were used as a stable pressure-velocity pairing which accurately models the quadratic velocity profiles and the linear pressure gradients [42]. Since the fluid flow has one-way coupling with the species transport, the laminar flow could be computed using a fully coupled nonlinear Newton method. For the smaller baseline cases, the PARDISO linear solver was used, which exhibited much faster convergence. For the SECP flow, the problem required a larger

amount of memory, so the iterative solver, GMRES accelerated by an algebraic multigrid, was used for its memory efficiency. The default tolerance of 0.001 was used for both fluid flow and species transport. Further increasing the tolerance did not meaningfully alter the result.

The mass transfer model was computed using the transport of dilute species interface (TDS) meaning the diffusion is approximated by Fick's law. The main quantity of interest was the normal diffusive flux. This quantity is a derivative of concentration, which is nonlinear in the mass boundary layer. Using linear elements results in a flux based on piecewise constant values, whereas using quadratic elements results in a flux based on linear functions. The quadratic elements were found to be more adept at representing the concentration profile accurately. As mentioned in Section 2.3.2, the developing concentration boundary layer is not axially periodic, so when modelling a single unit cell, the outlet concentration must be mapped back to the inlet. COMSOL does not natively support axial mapping of the outlet concentration to the inlet via the TDS interface, but this can be achieved using a general extrusion operator coupled to a boundary ODE to track the temporal evolution of the bulk concentration.

Radiation is computed using the same computational methods as presented in the KE section. The major differences are that only one wavelength is tracked, and the input radiation is either Lambertian or normal to the opening. A convenient workflow to map the radiation data from the full unit cell to the symmetric unit cell, used for flow modelling, is through an identity mapping, assuming they have the same spatial coordinates for each geometric unit. This was achieved using a general extrusion operator. Finally, it should be stated that COMSOL does not give direct access to deposited power as a boundary variable for use as an input to another simulation case. However, by using an accumulator on the boundary, which tracks how many rays strike an element face, coupled with the absorbed ray power as the source term, the deposited power field can be obtained and used elsewhere.

Mesh refinement studies were conducted on the highest Reynolds (5813) and Schmidt (1079) numbers examined since these are the most demanding cases. The cross-sectional velocity profile as well as the pressure drop was compared to literature data found in Shah and London [35] to validate the laminar flow for the flat plate and the baseline case. The mass transport cases were validated by comparing the average mass transfer coefficients to the model of Muzychka and Yovanovich [36]. Mapped swept structured meshes were used for both the baseline case and the

SECP reactor. For the SECP reactor, the body-fitted mesh was achieved using the mesh deformation interface. The use of this interface is effectively a workaround in COMSOL to create a mesh that follows the rounded curvature of the cavities and protrusions while avoiding highly skewed elements, especially at the cavity lip. This is done by specifying the cavity dimensions using parametric equations for a hemisphere. Finally, detailed methodology for meshing strategies can be found in the Appendix.

3 Results and Discussion

3.1.1 Kinetic Estimation

3.1.2 Flow Dependence

Prior to fitting kinetic parameters using the measured mass transfer coefficients and the full kinetic model, which incorporates the radiation effects directly, a simplified LH model (Equation 2.17 without the LASREA term), which lumps all effects into combined coefficients, k_0 and K_1, was solved to test the Reynolds number dependence. The datasets of the laminar Reynolds numbers (431, 782, and 1633) were tested under the same constant illumination intensity of 122 W m^{-2}. This theoretically means any change in 4-CP degradation should be solely due to the increased mass transport caused by the higher convective flow. The adsorption term K_1 was shared across all datasets, while the effect of mass transfer was lumped into the forward reaction coefficient, k_0. The graphical results of this kinetic fitting are presented in Figure 3.1 while the kinetic parameters are summarized in Table 3.1.

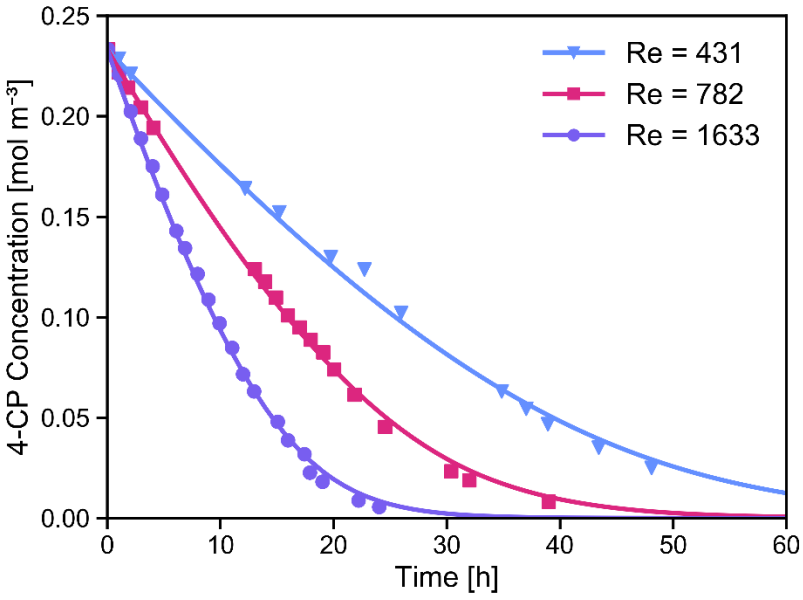


Figure 3.1. Kinetic fitting for the lumped parameter model under a perceived laminar flow regime.

Table 3.1. Summary of Reynolds-dependent kinetic parameters for the lumped parameter model.

Kinetic Parameter	Value
$k_{0,431}$ [mol m^{-2} s^{-1}]	1.36e-7
$k_{0,782}$ [mol m^{-2} s^{-1}]	2.18e-7
$k_{0,1633}$ [mol m^{-2} s^{-1}]	3.69e-7
K_1 [mol m^{-3}]	0.1

The dependence of the kinetic coefficients on the Reynolds number is plotted in Figure 3.2 and then fit to a power law model via Equation 3.1.

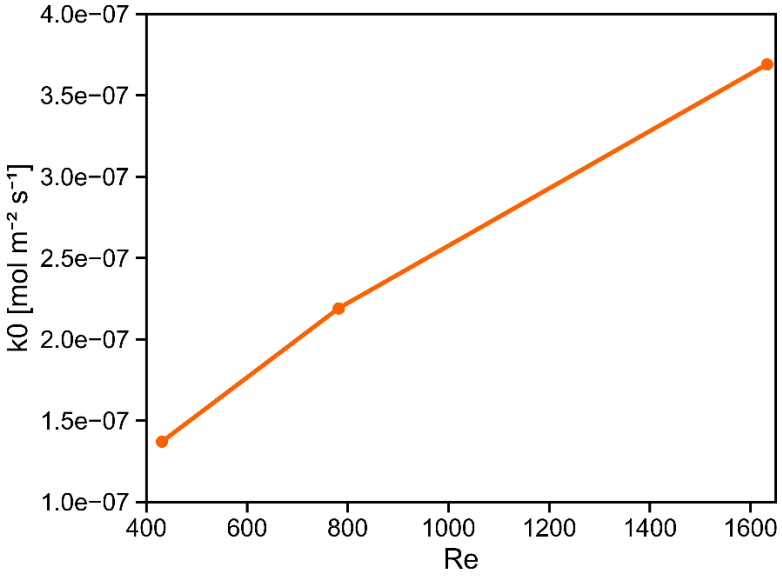


Figure 3.2. Reynolds dependence of the lumped kinetic parameters.

$$k_0 = 2.0e^{-9}Re^{0.7447} \tag{3.1}$$

The result of Equation 3.1 shows that the kinetic data varies with a Reynolds dependence of approximately 0.74. This scaling coefficient can be compared to the scaling coefficient derived from both the mass transfer coefficients using Equations 2.21-2.23 and those measured by Zhang [21] with Equations 2.25 and 2.26. The average mass transfer coefficients for 4-CP, assuming a smooth laminar duct under a developing concentration boundary layer, are summarized in Table 3.2. Notably, since the Schmidt number is high, the momentum diffuses much faster than the mass, so the Graetz flow solution closely matches the laminar boundary flow. Likewise, the measured data from Zhang are also reported in Table 3.2.

Table 3.2. Comparison of average mass transfer coefficient between the Muzychka and Yovanovich models versus the measured values from Zhang.

	$\bar{k}_{4CP}$ [m s^{-1}]	
Re	**M&Y [36]**	**Zhang [21]**
431	1.08e-6	2.29e-6
782	1.32e-6	3.87e-6
1633	1.69e-6	6.74e-6

The data of Muzychka and Yovanovich [36] in Table 3.2 follow the classical 1/3 power scaling for Graetz-type flows, which is expected. Conversely, the data measured by Zhang follow approximately a 0.81 power scaling with Reynolds number, which matches more closely to the trend exhibited in the kinetic data and to the Reynolds scaling of fully developed turbulent flow in internal flows [46]. There is a clear discrepancy between the experimental power scaling and the theoretical power scaling under the same flow regime. The most likely reason for this variation is due to the flow distributor near the reaction zone. It is known that the packed bed has 5 mm glass beads that attempt to straighten the inlet flow; however, this may have caused undesired flow paths close to the duct boundary or pore jets, which can disrupt the boundary layer, leading to higher mass transfer coefficients. Only the bead diameter is known, but physical plausibility can still be checked by making some assumptions about the packed bed. With the known bead diameter, the particle Reynolds number can be computed using the superficial velocity for the lowest value of 431, yielding approximately 56.6. Beds with random packing typically have porosities around 0.35-0.45 [47], so using the highest porosity yields an average interstitial particle Reynolds number of 126 at the minimum. Experiments have shown a loss of laminar behaviour with interstitial particle Reynolds numbers in the range of 90-120 [48], so despite uncertainty regarding the packed bed, we can assume a loss of laminar behaviour as a potential source of higher mass transfer. This is supported by the fact that the packed bed proximity was very close to the reaction zone, which itself is only 0.5 m long, so it is not physically unrealistic to assume that the turbulent effects do not dissipate appreciably over that short reactor length.

3.1.3 Radiation Field

A contour of the LASREA field on the film surface assuming a total input of 1 W is given by Figure 3.3. Recall that the input power of 1 W is specified as a convenient reference value to easily scale the field with the varying intensity. The total area open for radiation for the flat plate is 0.04 m^2.

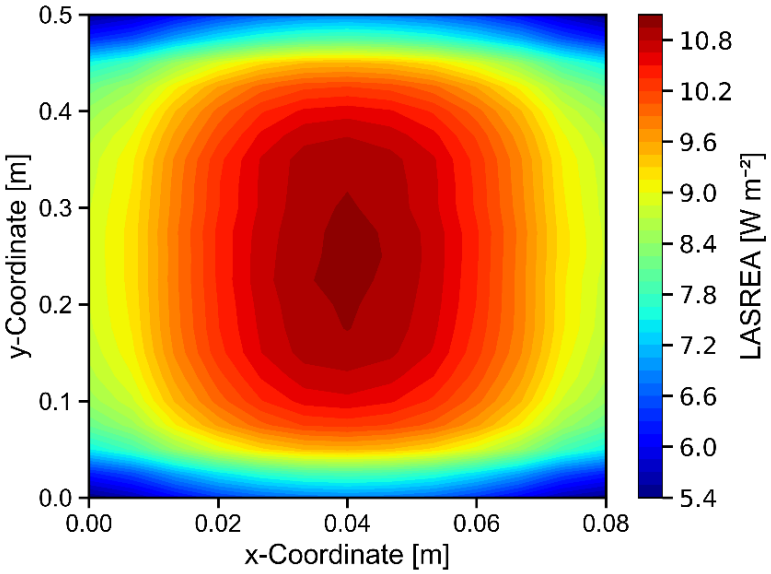


Figure 3.3. LASREA field at the film surface for the flat plate geometry under diffuse radiation. The x and y-coordinates represents the reactor width and length consistent with Figure 2.1.

In Figure 3.3, the radiation field follows an expected pattern based on geometrical optics. Higher absorbed power is concentrated towards the center of the film. Towards the edges, the rays have a higher angle of incidence, meaning the intensity drops off at these oblique angles due to the cosine law. The LASREA is lower than the externally applied power due to several losses. Some rays are lost passing through the transparent walls as well as the inlet and outlet openings. There is attenuation due to the light absorption in the plexiglass cover. The film is not a perfect blackbody, so many of the spectral rays are reflected and potentially lost. Lastly, some rays are completely reflected out of the domain at the material interfaces due to the difference in refractive index.

3.1.4 Parameter Estimation

The estimated kinetic parameters obtained from the nonlinear least squares are transformed back from their logarithmic or reciprocal logarithmic form into parameters consistent with Equation 2.17. The intrinsic parameters are summarized in Table 3.3.

Table 3.3. Summary of the fitted kinetic parameters for the full LH model.

Kinetic Parameter	Value
k_0 [mol m^{-2} s^{-1}]	6.34E-05
K_1 [m^3 mol^{-1}]	34.025
K_2 [m^3 mol^{-1}]	0.0035

The results of the Reynolds dependence fitted with the newly fitted parameters are given by Figure 3.4. The accompanying surface concentration profiles of both 4CP and oxygen are presented in Figure 3.5 and Figure 3.6.

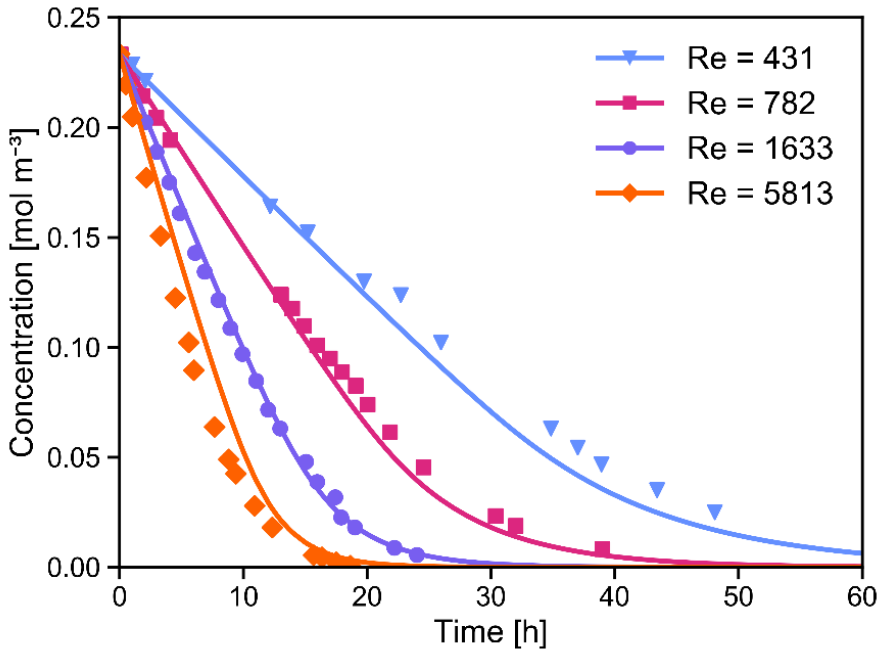


Figure 3.4. Model predictions compared with the experimental data showcasing the effect of Reynolds numbers on the degradation rate of 4-CP. Input intensity is 122 W m^{-2}.

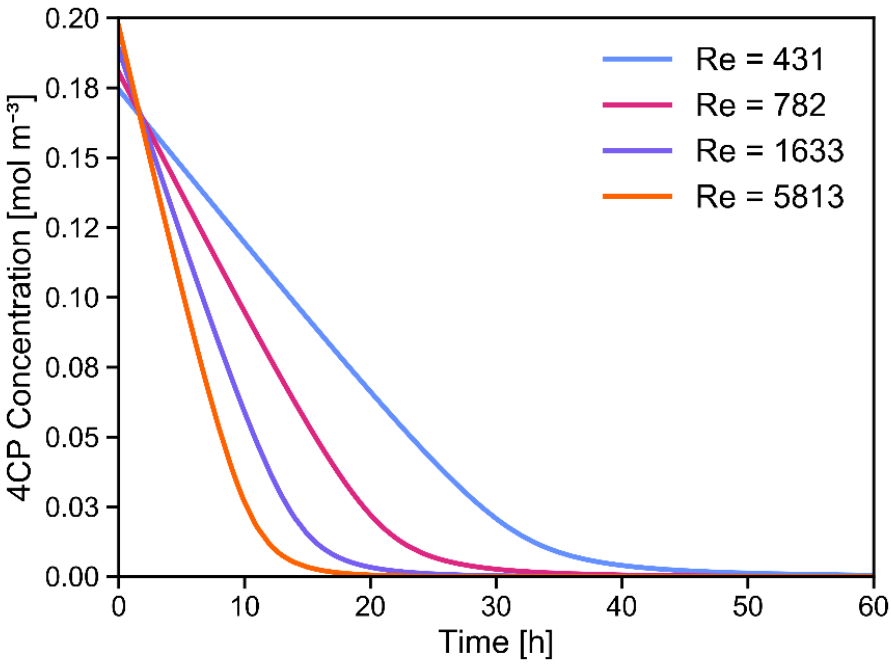


Figure 3.5. 4-CP surface concentration profiles under various Reynolds numbers. Input intensity is 122 W m^{-2}.

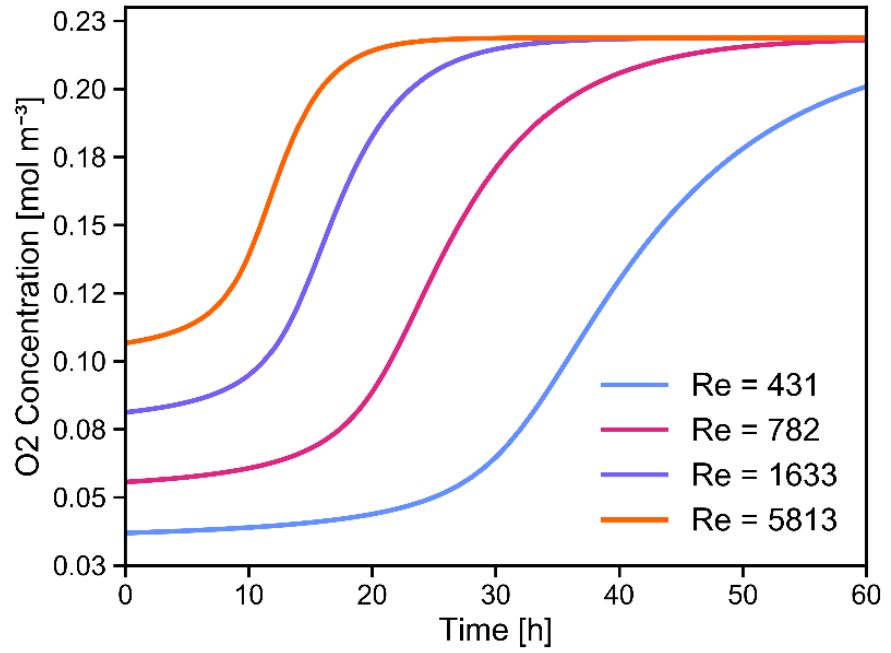


Figure 3.6. Oxygen surface concentration profiles under various Reynolds numbers. Input intensity is 122 W m^{-2}.

Figure 3.4 shows very good agreement between the fitting model and the experimental data when the mass transfer coefficients measured by Zhang [21] were used. The results of this figure represent a decoupling of the mass transfer unlike the results of Figure 3.1 as those results allowed the mass transfer coefficient to vary freely. As the Reynolds number is increased, the degradation time is shortened, which suggests the system is in the mass transfer-limited regime. As the 4-CP concentration tends towards zero, at the same time the surface oxygen spikes towards its bulk saturation value. This indicates that at that time, 4-CP depletion now governs the rate. Oxygen recovery occurs sooner with higher Reynolds number due to the faster transport. Based on the results of the surface concentration plots, mass transfer still limits the rate, which makes physical sense since the intensity is high.

Based on the discussion in section 3.1.1, any attempt at fitting the model using the theoretical laminar mass transfer coefficients was unsuccessful. The results of those sensitivity tests showed that under laminar mass transfer, the supply of oxygen was too slow to keep up with the great demand for full oxidative mineralization of the parent compound. As such, it led to unphysical surface concentrations.

The radiation dependence fitted with the regressed parameters is given by Figure 3.7. Once again, the surface concentration profiles under varying radiation intensities are given by Figure 3.8 and Figure 3.9 respectively.

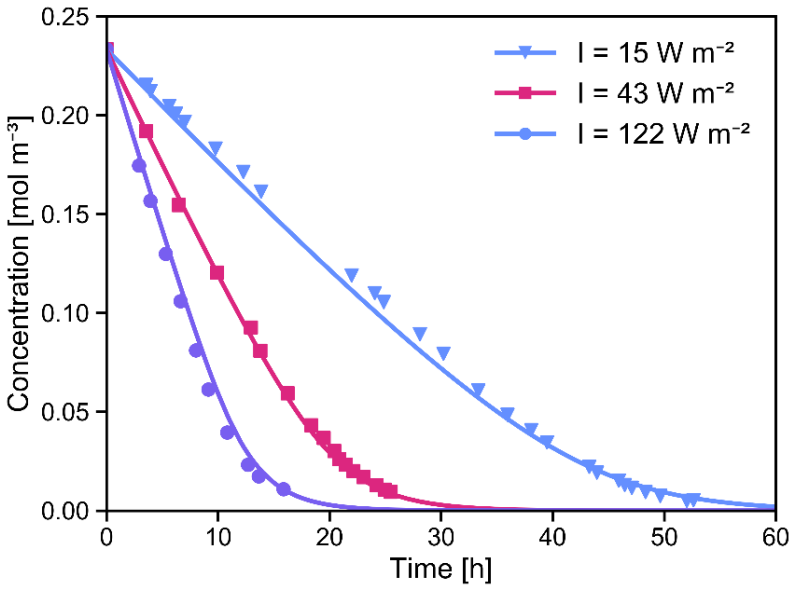


Figure 3.7. Model predictions compared with the experimental data showcasing the effect of intensity on the degradation rate of 4-CP. Reynolds number is constant at 4314.

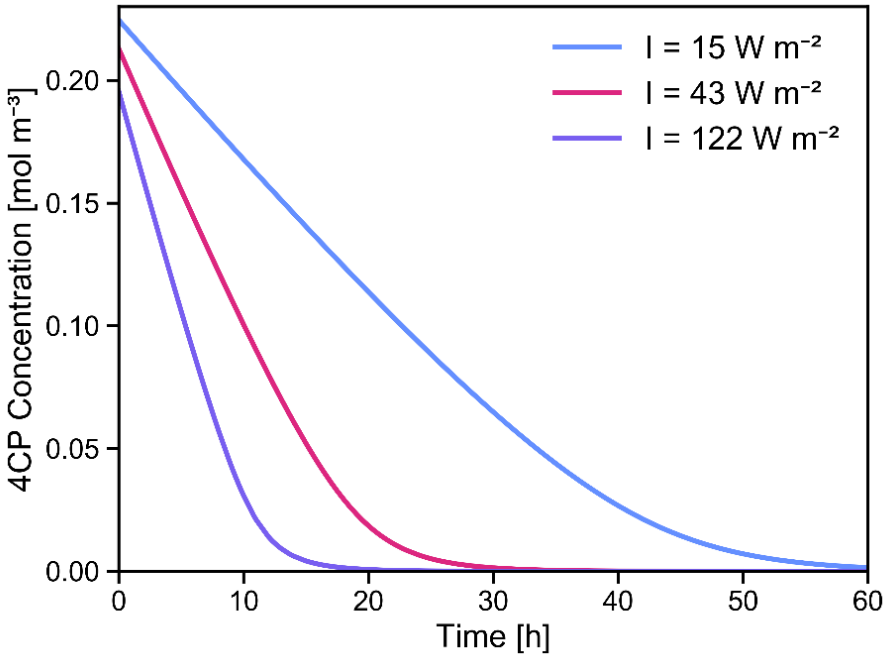


Figure 3.8. 4-CP surface concentration profiles under various intensities. Reynolds number is constant at 4313.

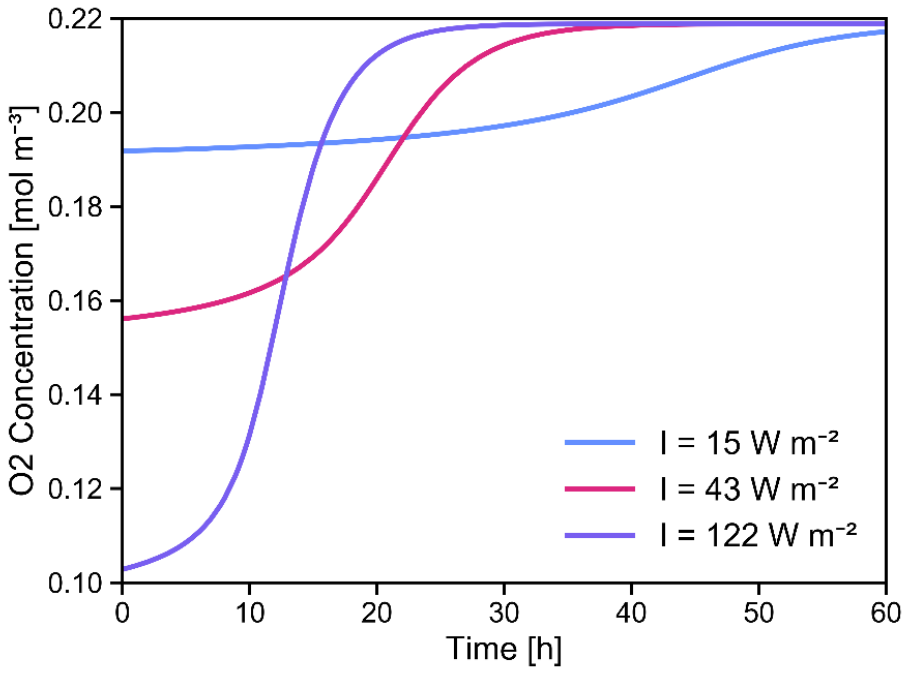


Figure 3.9. Oxygen surface concentration profiles under various intensities. Reynolds number is constant at 4313.

Since the Reynolds number was held constant, yet the degradation time decreased with increasing intensity, this suggests that the system is photon-limited at this flow rate. Theoretically, higher intensity generates more reactive charge carriers, which can then consume more of the reactants [10,49]. This stronger illumination accelerates the surface reaction, causing lower surface oxygen due to the higher consumption demand. The same rapid oxygen recovery trend is seen when 4CP is consumed and the lack of it fully controls the rate. The light parameter, n, was varied manually throughout fitting and a linear dependence of 1.0 was found to fit the data the best. This is consistent with previous studies on the light dependence of photocatalytic surface reactions [23,50,51]. Mechanistically, at sufficiently low photon flux, electron-hole generation is low enough to render the recombination rate negligible in comparison [50]. Therefore, increasing the absorbed photon flux increases the population of useful photogenerated charge carriers, which increases the rate proportionally. As the intensity is increased, electron-hole recombination becomes increasingly dominant, and the rate starts to scale sublinearly, with a transition toward a square-root dependence at high enough intensities [23]. While the definition of low-intensity regions is highly system-dependent, a low-intensity range that is commonly cited is approximately 0-200 W m^{-2} [51]. This range of intensities falls well within this range.

Examining the kinetic parameters directly shows that the oxygen adsorption term is very low relative to its concentration. This suggests that oxygen is never fully saturated on the catalyst surface during the reaction. This is seen clearly in the oxygen surface concentration plots of Figure 3.6 and Figure 3.9 where oxygen always remains lower than its bulk concentration when there is a high enough supply of 4-CP. As such, the model approaches a first-order dependence for all oxygen concentrations in this range of parameters. This is consistent with the low adsorption coefficient found by Mills et al. [31]. The summary of the final kinetic parameters consistent with the reduced model of Equation 3.2 is given in Table 3.4. This reduced model with these parameters is used in the subsequent base case and SECP modelling.

$$r''_{4CP} = \frac{k_0^* K_1 C_s O_s}{(1 + K_1 C_s)} \left(\frac{q}{q_{ref}} \right)^n \tag{3.2}$$

Table 3.4. Summary of kinetic parameters for the reduced model.

Kinetic Parameter	Value
k_0^* [m s^{-1}]	2.21E-07
K_1 [m^3 mol^{-1}]	34.025

3.1.5 Surface-Enhanced Corrugated Plate

3.1.6 Flow Structures

We start with the baseline case to allow for comparison of the flow structures and isolated mass transfer effects. The contour of the flow profile for the unmodified corrugated plate photoreactor is given by Figure 3.10.

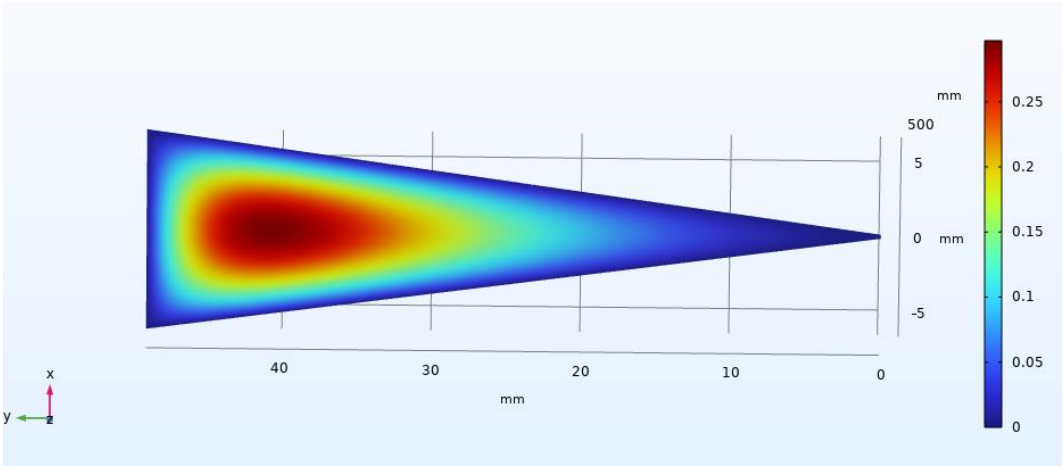


Figure 3.10. Contour showcasing the cross-sectional velocity profile for the unmodified triangular duct. The colour bar is the velocity magnitude in m s^{-1}.

Additionally, the accompanying centerline velocity profile is compared to the analytical results of Shah and London [35] is given by Figure 3.11.

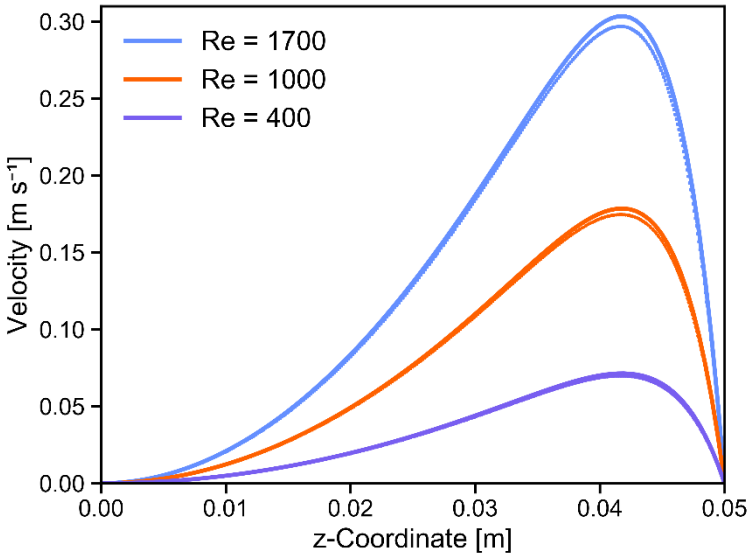


Figure 3.11. Centerline velocity profile plotted with the analytical results computed by Equation 2.34.

The velocity profile in Figure 3.10 shows very low velocity near the tip and a much higher core velocity closer to the top of the duct. The low velocity is due to the high viscous forces dominating due to the presence of the walls at the tip. Naturally, the maximum velocity occurs at the centroid of the duct where the flow is relatively far from all walls. The velocity profiles in Figure 3.11 are in close agreement, which validates the numerical results. There is a slight

difference in the maximum velocity, which is more pronounced at the higher flow rate. This is most likely due to the truncation of the tip, which causes additional viscous shear locally at the bottom of the duct. This change propagates through the profile, resulting in a slightly lower maximum velocity than the analytical solution. This slight difference is still valid for the comparison test since the SECP reactor also has this truncation, but a better method of meshing while preserving the velocity profile was thought of after the fact. Ideally, it would be better to partition the tip and apply an unstructured mesh in this low-flow region while using the newly added edge from the partition to create the structured quad mesh.

The local profile of mass transport via the normal diffusive flux is given by Figure 3.12. The highest Reynolds number tested (1700) is plotted, but the trend remains similar across all runs.

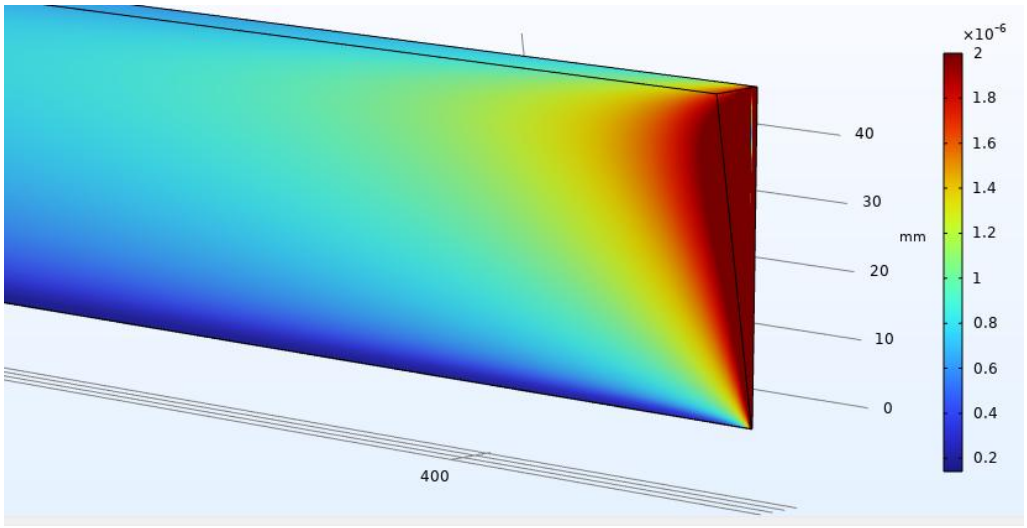


Figure 3.12. Normal diffusive flux profile in mol m^{-2} s^{-1} on one half of the symmetric film boundary. The max flux is manually set to 2E-07 mol m^{-2} s^{-1} to visually accentuate the entrance effect and the local differences caused by the geometry.

The local profile of the normal diffusive flux shown in Figure 3.12 is physically consistent with the fully developed flow field. At the entrance, the mass boundary layer is the thinnest since the near-wall concentration is equal to its inlet value near the wall. As the length increases and the species is consumed at the reactive film, a concentration gradient is formed. Continuing downstream increases the time for molecular diffusion to propagate the effect of the reactive wall to the bulk fluid. The flux profile shows higher normal diffusive flux closer to the centroid core of the duct where the fluid velocity is at its maximum. Conversely, near the apex of the duct, the flow

is much slower, resulting in slower mass transport. This is consistent physically since regions of high convection replenish higher-concentration fluid closer to the thin mass boundary layer.

The average mass transfer coefficients for this duct are compared against previous cases done on a flat plate, as well as corrugated reactors with less triangular ducts. Notably, these were only done for comparison purposes, and all geometries use the same global reactor dimensions consistent with Figure 2.1. Furthermore, the average coefficients are also compared against the prediction of the Muzychka and Yovanovich [36] model. The results are presented in Figure 3.13.

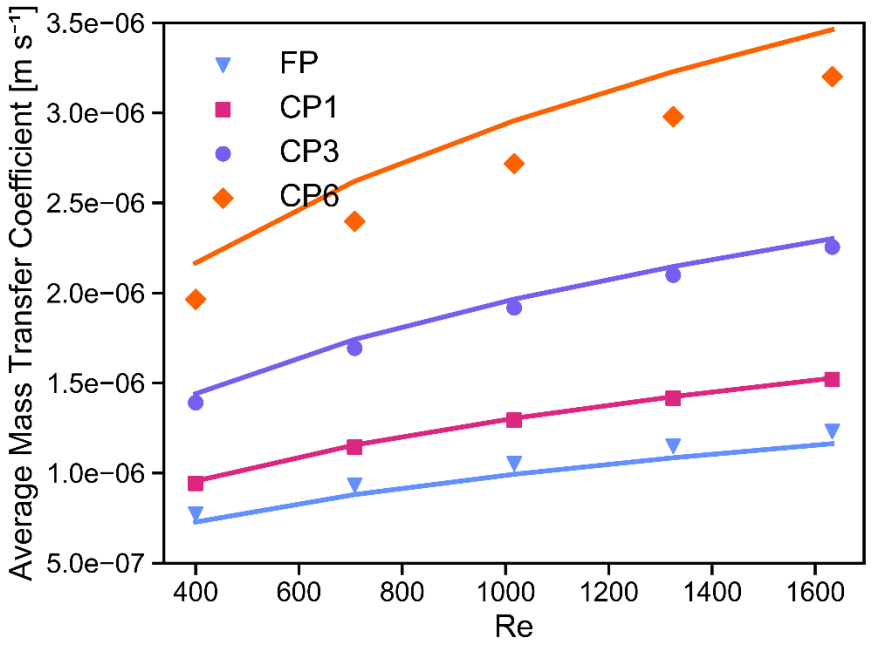


Figure 3.13. 4-CP average mass transfer coefficients with varying Reynolds number. CFD and model predictions for a flat plate and corrugated plates with varying apex angles (defined using number of ducts) are presented.

The numerical and literature results of Figure 3.13 are all within ±10% of the model predictions. The largest deviation is seen with the smallest apex angle. This is most likely where the model starts to become more uncertain since the available experimental data in Shah and London [35] for low aspect ratios becomes fewer. The Reynolds dependence in the plot exhibits the well-known 1/3 scaling for Graetz-type laminar flow [35,36,46]. The effect of decreasing the aspect ratio (equivalent to decreasing the apex angle) shows higher mass transfer in narrower ducts. This is supported physically by the flow field, since a narrower duct causes higher shear due to the larger near-wall gradient. As a result, the mass boundary layer becomes thinner, leading to a larger

normal diffusive flux. Finally, for completion's sake and for comparison with the SECP, the pressure drops for the baseline case compared with Shah and London [35] are presented in Table 3.5. Again, there is very good agreement between the calculated values and the literature data.

Table 3.5. Pressure drop comparison to literature data for calculated pressure drops for the base case.

		ΔP [Pa]	
Re	**Q [m^3 s^{-1}]**	**Shah and London**	**CFD**
400	9.59E-06	2.31	2.27
1000	2.40E-05	5.77	5.68
1700	4.08E-05	9.82	9.66

We now begin the discussion of the protrusion flow structures. The bulk flow in the unit cell is effectively the same profile as the base case. The flow near the wall for the top dimple for the largest Reynolds case ran of 1796 is given in Figure 3.14.

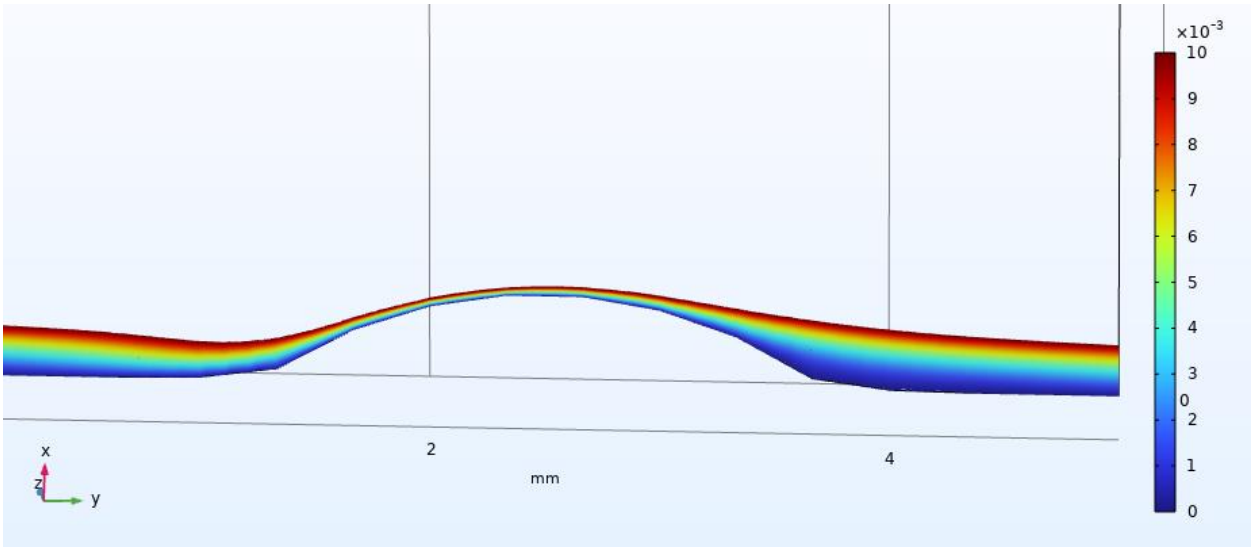


Figure 3.14. Flow streamlines for the near wall flow over a protrusion. Color bar gives the fluid velocity in m s^{-1}.

Under the highest Reynolds number of 1796 tested, the fluid profile moves with the curvature of the protrusion. The fluid boundary layer does become thinner at the top since the flow accelerates. As the flow passes over the protrusion a small wake is generated behind it given a thicker flow boundary layer. The consequence of this with regards to increasing mass transfer is most likely

higher mass transfer at the top since the normal gradient is higher, but lower mass transfer directly behind the protrusion.

Moving on to the dimples. The unit cell also exhibits similar bulk flow velocity as the base case, but near the dimple structures is where differences reside. Streamlines cutting through the middle of several dimples at varying positions along the duct height are given by Figure 3.15, Figure 3.16, and Figure 3.17 respectively. The Reynolds number for each is constant at the highest in the range (1796).

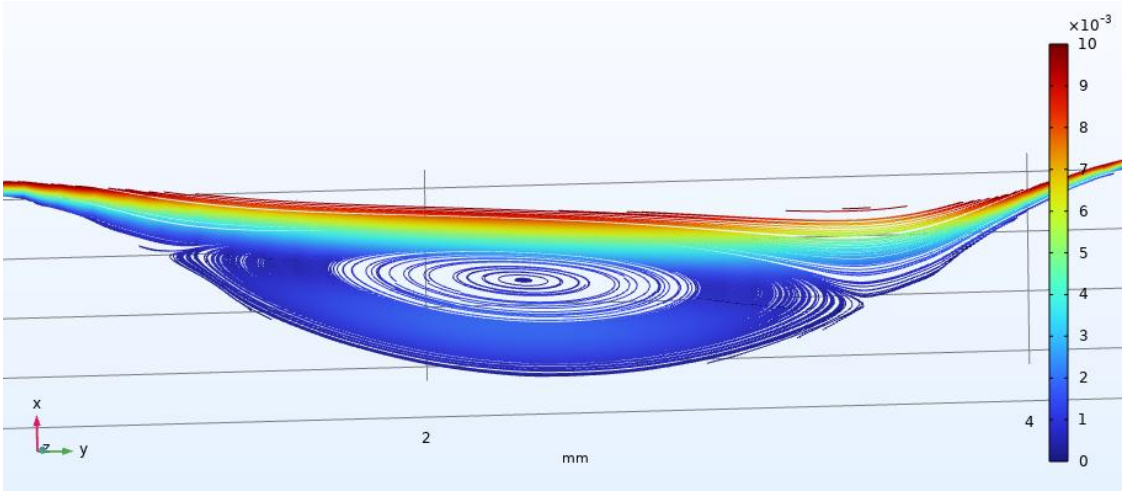


Figure 3.15. Velocity streamline (Re = 1796) at the top dimple where the bulk velocity is near its maximum. A large recirculation zone is observed which pushes back the flow re-attachment point. Color bar gives the fluid velocity in m s^{-1}.

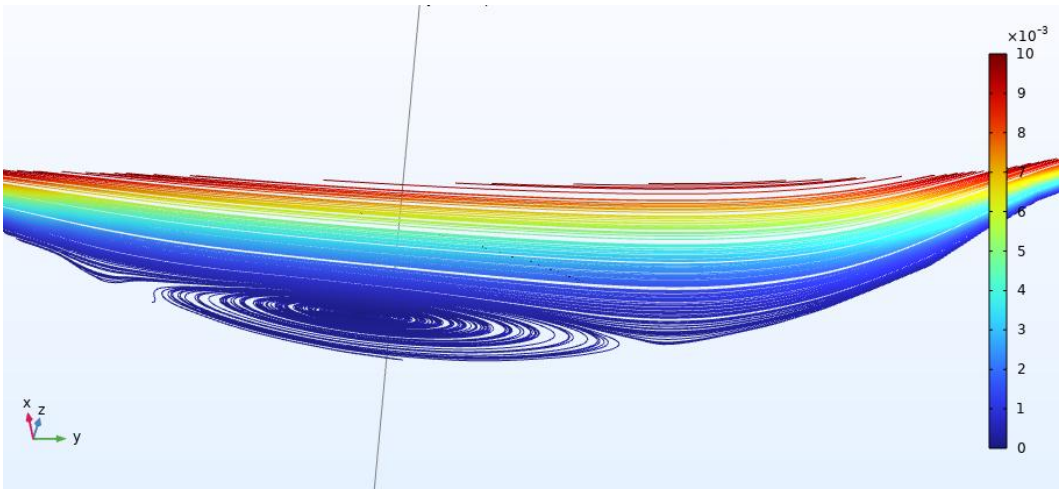


Figure 3.16. Velocity streamline (Re = 1786) at the 4th dimple where the bulk velocity has reduced. A smaller recirculation zone is observed. The flow re-attachment point is now further down the dimple. Color bar gives the fluid velocity in m s^{-1}.

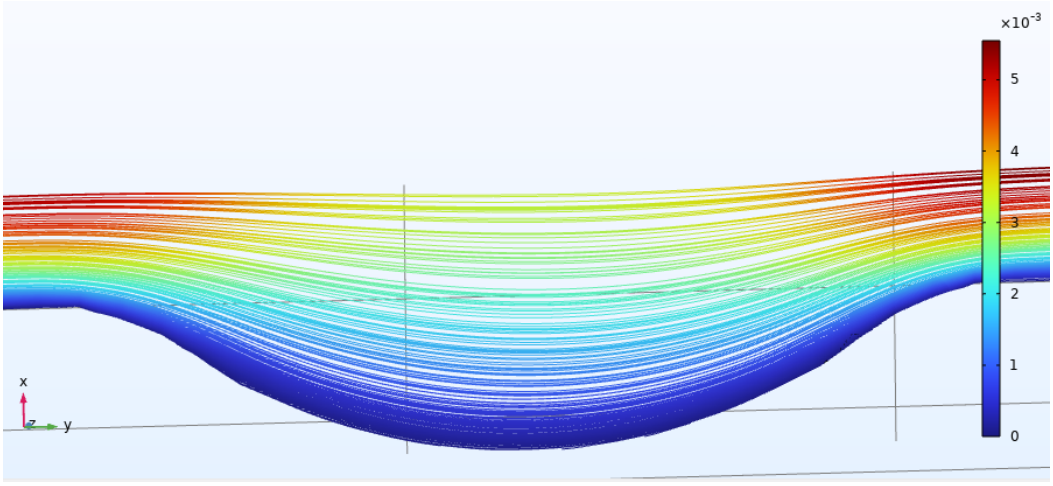


Figure 3.17. Velocity streamline (Re = 1786) at the 9th dimple where the bulk velocity is very low. No recirculation zone is observed. The flow follows the dimple curvature. Color bar gives the fluid velocity in m s^{-1}.

The series of plots show a decrease in the size of the recirculating zone at lower points in the triangular duct. Starting from the top there is a very large recirculation zone that formed. The fluid bulk velocity at this point in the triangular duct is large enough that fluid parcels have enough appreciable momentum to separate from the bulk flow when the sudden opening is encountered. This creates a separated shear layer that drives fluid into the cavity creating a vortex. As the bulk velocity decreases down the duct, the size of the recirculation zone starts to decrease as well due to lower momentum in the fluid. Near the bottom of the duct (Figure 3.17) the fluid velocity is low

enough that viscous force dominate completely and the flow can follow the curvature of the dimple. Finally, the summary of pressure drops for each Reynolds number investigated is given in Table 3.6.

Table 3.6. Comparison of dimple pressure drops to the base case.

		ΔP [Pa]	
Re	**Q [m^3 s^{-1}]**	**Base Case**	**SECP**
182	9.59E-06	1.04	1.00
904	2.40E-05	5.77	5.00
1796	4.08E-05	10.37	10.00

The pressure drops are quite comparable. While the dimpled flow has slightly lower pressure drop, but it is not substantial at this low flow rate.

3.1.7 Radiation Profiles

Beginning with the baseline case to examine the effects of diffuse radiation input compared to normal input. The reference LASREA contour plots with their accompanying surface line plots for both the diffuse and normal inputs are given by Figure 3.18 and Figure 3.19 as well as Figure 3.20 and Figure 3.21 respectively.

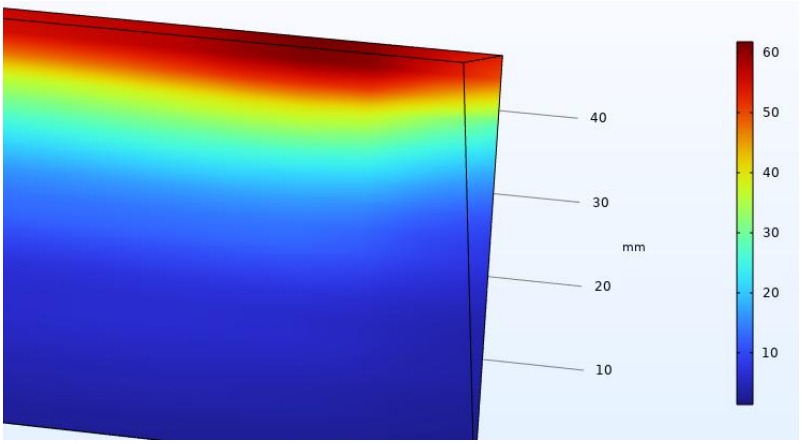


Figure 3.18. LASREA contour for the base case under a diffuse radiation source. The color bar shows the reference LASREA magnitude in W m^{-2}.

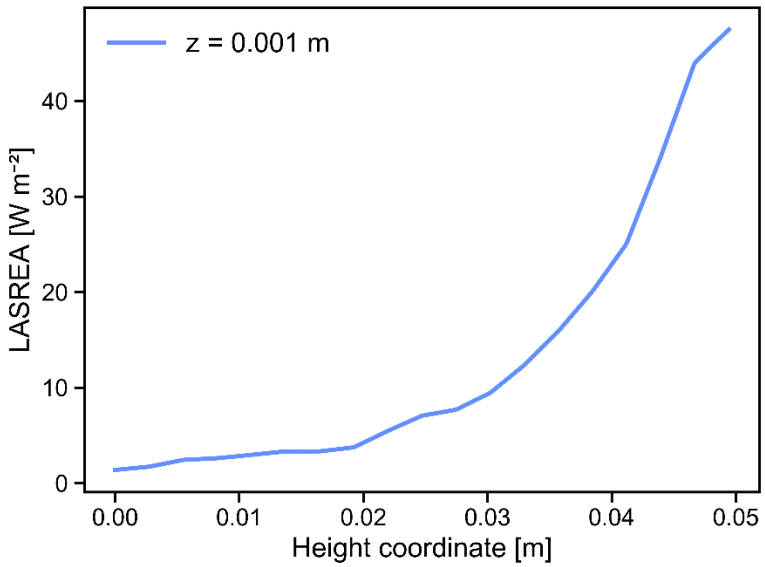


Figure 3.19. LASREA profile for the base case under a diffuse radiation source. 0.05 m corresponds to the top of the duct.

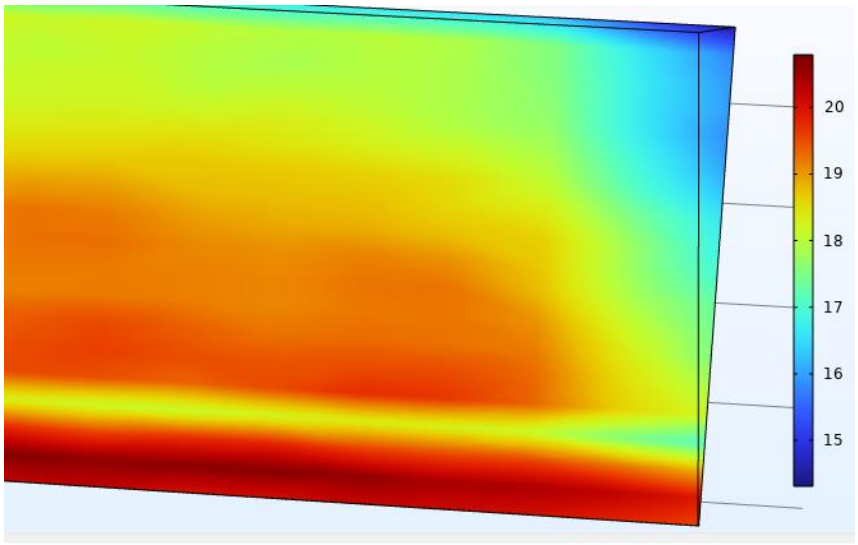


Figure 3.20. LASREA contour for the base case under a normal radiation source. The color bar shows the reference LASREA magnitude in W m^{-2}.

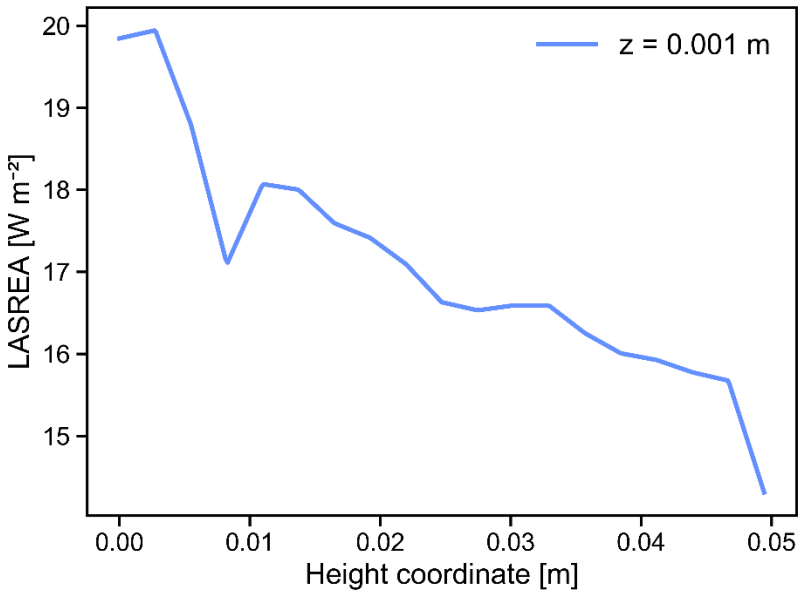


Figure 3.21. LASREA profile for the base case under a normal radiation source. 0.05 m corresponds to the top of the duct.

The diffuse radiation contour in Figure 3.18 is physically consistent with the profile seen in the KE diffuse plot. The incoming rays are biased closer to the top edges of the triangular duct since the hemispherical distribution in the Lambertian model has more rays entering at oblique angles. The LASREA profile in Figure 3.19 shows a decreasing trend along the reactor height. At the top of the duct, most rays in the distribution hit the top half of the duct surface. All these rays are then reflected diffusely. These reflections near the top have a high chance of being reflected out of the domain due to the proximity to the opening. Near the bottom of the duct, the absorbed power starts to dramatically decrease. This is primarily because only 3% of the rays in a Lambertian distribution are within 10° of the perpendicular surface angles. This means that only a small fraction of the rays can reach the bottom of the duct since they are more likely to hit a portion of the angled surface earlier and be reflected towards the top surface and eventually out of the opening.

Unlike the diffuse profile, the normal profile of Figure 3.21 shows a more uniform distribution with LASREA values ranging from approximately 14 to 20 W/m^{-2} over the entire film. Since all rays are travelling perpendicular to the opening, a much larger portion of rays can reach deeper into the triangular duct. Once these rays reach the bottom, since the apex angle is small, the rays can then undergo multiple closely bound reflections. This reflection effect is exhibited in Figure

3.20 since the bottom portion near the tip receives the largest portion of absorbed intensity. Travelling up the duct shows a loss in absorbed radiation. This is caused by less of the distribution being at oblique angles from the initial release point. However, the difference is not as stark as the diffuse profile since rays undergoing reflection from the tip have a larger chance of being reflected up to the top surfaces prior to being reflected out through the opening. Lastly, some numerical noise is seen in the plots, which is caused by a sampling artifact and potentially too coarse a mesh.

From the results of the base case, the normal radiation profile had a more positive effect on the degradation compared to the diffuse source. As such, the normal model is chosen to compute and compare the radiation profiles for the surface modifications. Starting with the protrusions, the contour of the reference LASREA field for the protrusions under a normal radiation input is given by Figure 3.22.

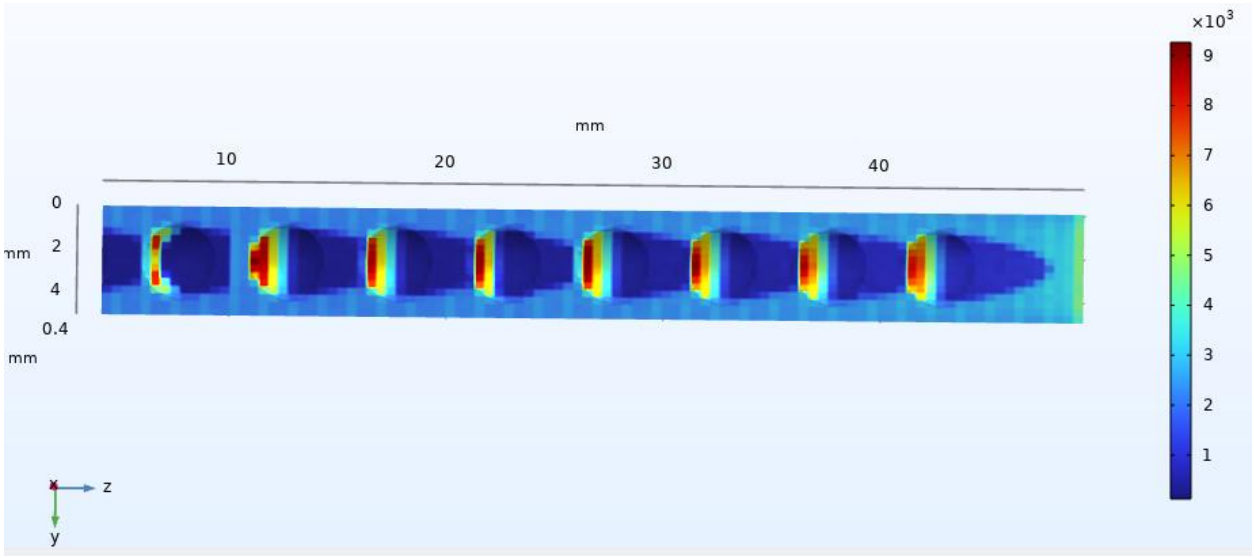


Figure 3.22. Contour of the reference LASREA using a normal radiation source over the angled surface modified with protrusions. The axis angle is set so that the radiation rays enter parallel from left to right. The color bar shows the reference LASREA magnitude in W m^{-2}.

From Figure 3.22 the addition of protrusions causes localized hotspots under a normal radiation source. As the rays enter, they are most likely to hit the top of the protrusion first and undergo reflection. The high depth value for the cavities, which becomes a high height value for the protrusions, causes clear shadowing. The top of each protrusion blocks the rays from reaching the backside. Consequently, the resulting radiation field is highly nonuniform, which would most

likely lead to reduced degradation performance. A potential fix would be to attempt to use shallowed protrusions, as that could lead to less self-shadowing.

The reference LASREA field for the dimple is given by Figure 3.23.

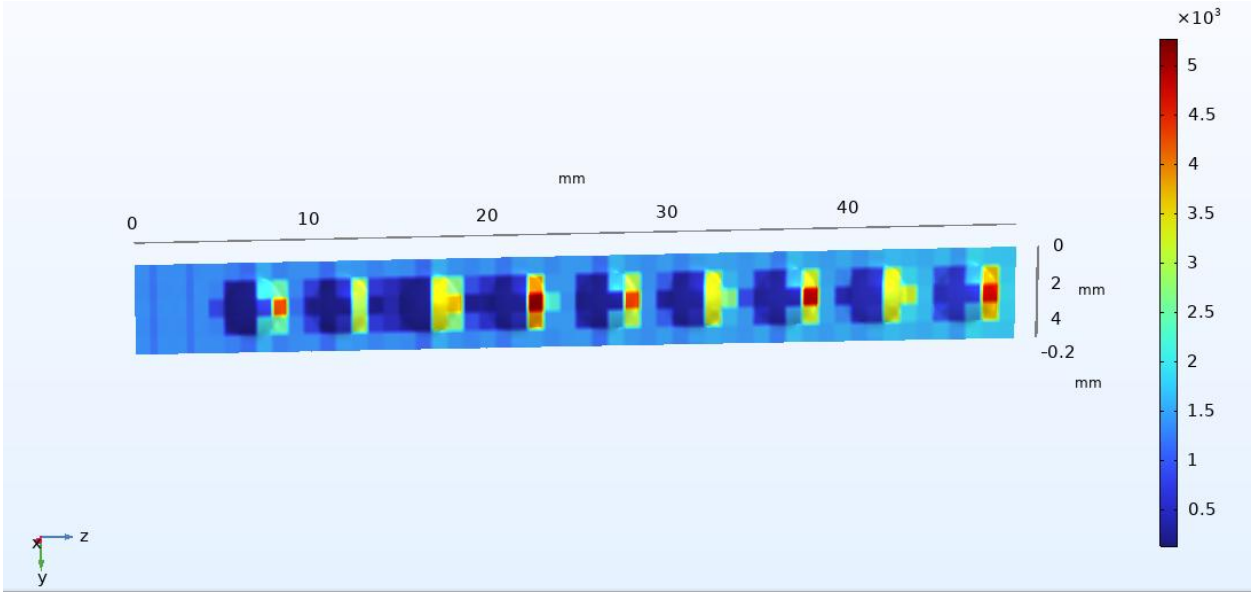


Figure 3.23. Contour of the reference LASREA using a normal radiation source over the angled surface modified with dimples. The axis angle is set so that the radiation rays enter parallel from left to right. The color bar shows the reference LASREA magnitude in W m^{-2}.

It is clear from Figure 3.23 that the dimple suffers from a similar shadowing effect as the protrusions. The dark interior at the top of the dimples is caused by the rays being intercepted by the rim before they could reach the top of the cavity. Potentially more oblique release angles could bias the rays deeper within the cavity. The consequence of this kinetically is twofold. On one hand there will be low reaction rates within the shadowed half of the dimples due to the low photon flux. On the other hand, there will be higher reaction rates on the bottom portion of the cavity. Assuming the dimples create some mass transfer enhancement the overall rate could increase. Finally, the dimples do suffer from spatial smearing due to the mesh element size; but the general trend should remain the same even with a finer mesh.

3.1.8 Degradation Performance

The main degradation metric used to track the performance of both the baseline case, and the SECP configuration is the total consumption of 4-CP over the entire reactor length. This is taken as the integral of the normal diffusive flux over the reactive film and represents the total molar consumption per pass of the reactor. The second metric used is an extension of this and is

simply the ratio of total molar consumption under a diffuse radiation source versus a normal source. To save time computationally, the full combined reaction model is only done on the baseline case to test this effect. We begin by examining the performance plots for the baseline case under varying Reynolds numbers and input intensities. The degradation performance plots for the baseline case under a diffuse radiation source and a normal radiation source are given by Figure 3.24 and Figure 3.25, respectively.

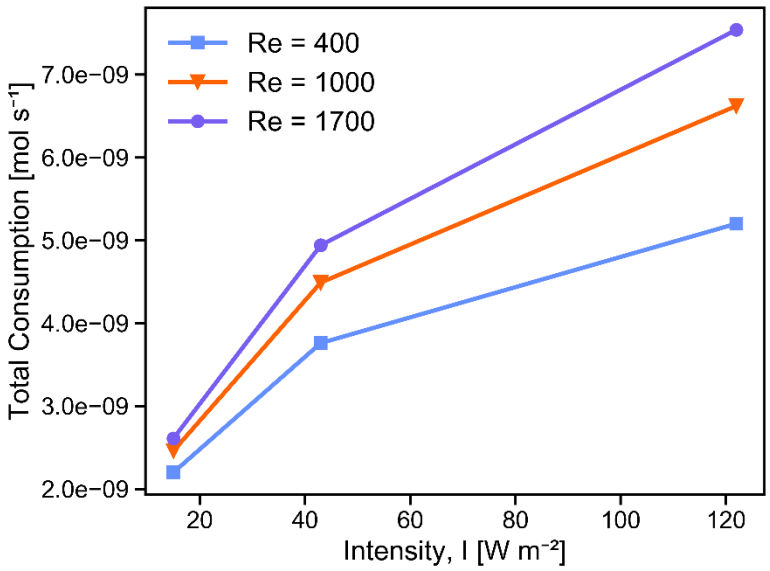


Figure 3.24. Total consumption of 4-CP for the baseline case under a diffuse radiation source as well as varying Reynolds numbers and input intensities.

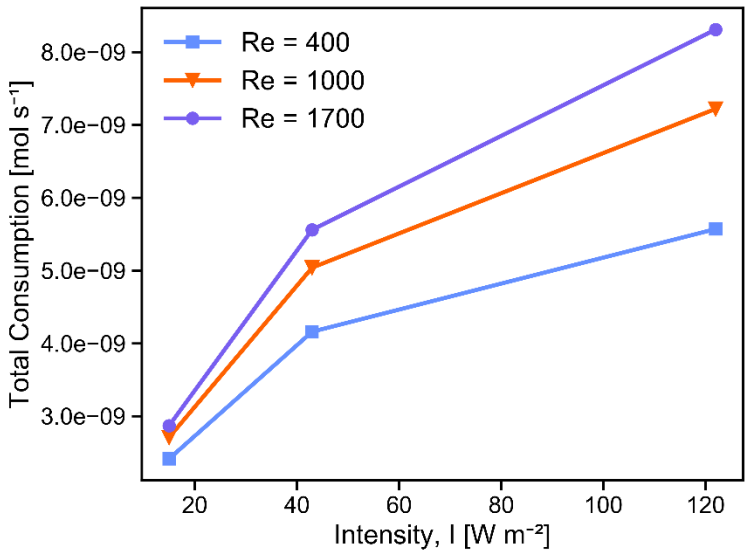


Figure 3.25. Total consumption of 4-CP for the baseline case under a normal radiation source as well as varying Reynolds numbers and input intensities.

Both Figure 3.24 and Figure 3.25 show similar upward trends as the radiation intensity is increased. The rate is a linear function of the absorbed intensity at this low-intensity range, so increasing it has a proportional effect on the rate, which is observed in the total consumption trend. The effect of increasing the Reynolds number, which is equivalent to higher convective transfer, has a physically consistent coupling with the intensity. At low intensities, the rate is kinetically limited by the absorbed photon flux, so increasing the Reynolds number has little effect on the overall degradation rate. As the intensity is increased, the effect of mass transfer becomes more pronounced. Under sufficient photon flux, there is a clear shift into a mass transfer-limited regime. Higher convective transport increases the reaction rate since the rate is now limited by the surface concentration of reactants supplied to the film by near-wall diffusion. At the highest intensity of 122 W m^{-2}, this effect is largest since the photon flux is more than sufficient.

The deviation between the plots is primarily in the magnitude of the consumption loss, which is consistent with the linear increase in the rate with increasing low intensities. Based on the LASREA plots shown previously in Figure 3.18 and Figure 3.19, the diffuse radiation source produces a more nonuniform LASREA field. The consequence of this kinetically is that most of the bottom surface does not actively participate in the reaction due to a lack of light exposure. On the other hand, the normal field produces a much more uniform spatial LASREA field, which allows more of the reactive surface to receive adequate light exposure. This thereby increases the

overall consumption over the entire reactor length. The quantified difference between these fields is given by Figure 3.26.

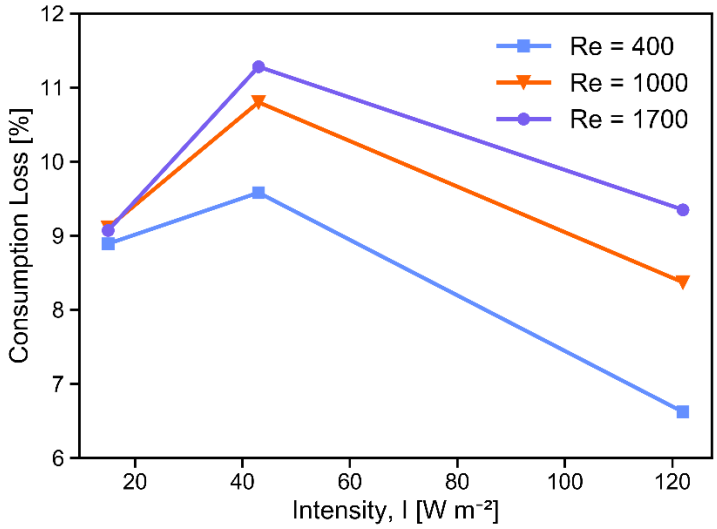


Figure 3.26. Total consumption loss of using a diffuse radiation source compared to a normal radiation source.

In Figure 3.26 the magnitude of the consumption loss is at most roughly 11.5% at the mid-tier intensity. This relatively low difference in the consumption loss is attributed to mass transfer limitations caused by the triangular geometry. Even with higher absorbed power spread more evenly over the film, not all areas are favoured transport-wise. Recalling Figure 3.12, the region closer to the apex of the duct has lower transport due to the low flow exhibited in Figure 3.10. Adding higher radiation in a region where the surface concentrations are low due to the transport does not add much benefit. It is most likely that the normal field allowed the middle portions of the duct to more favourably use their local mass transfer conditions, with the higher absorbed power resulting in a higher overall degradation rate. It makes sense that the moderate intensity of 43 W m^{-2} has the largest consumption loss since it represents a transition between the coupled mass transfer effects and absorbed intensity. As the intensity increases and mass transfer starts to become more limiting, the effects of a more uniform intensity field start to decrease. Future studies would benefit from a larger range of intensities to see exactly when that transition occurs.

Prior to continuing with the SECP geometry, it should be stated since it is quite computationally intensive to run these cases, only the combined mass transfer and radiation effects of the cavities are run to completion. Future work would be to run the full model to completion for

both geometries. The total consumption plot for the Reynolds numbers tested and varying intensities for the dimple SECP is given by Figure 3.27. The normalized 4-CP surface concentration is at the last unit cell to alleviate any entrance influence on the mass boundary layer. The highest Reynolds number of 1796 as well as the minimum and maximum intensities in the range are given by Figure 3.28 and Figure 3.29 respectively.

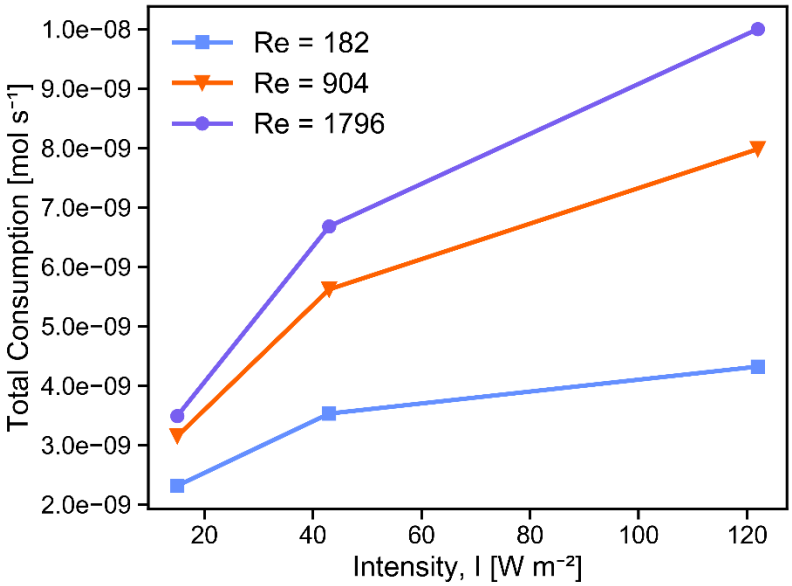


Figure 3.27. Total consumption of 4-CP for the dimple SECP case under a normal radiation source as well as varying Reynolds numbers and input intensities.

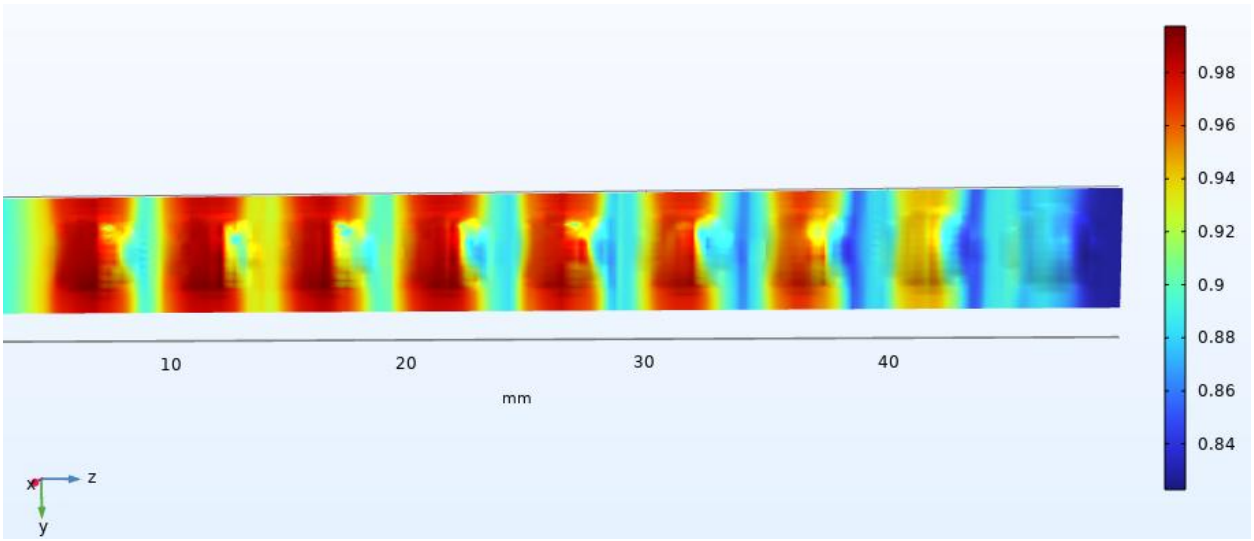


Figure 3.28. Normalized surface concentration (colour bar) on the catalyst film at the 100th unit cell. Re = 1796 and I = 15 W m^{-2}.

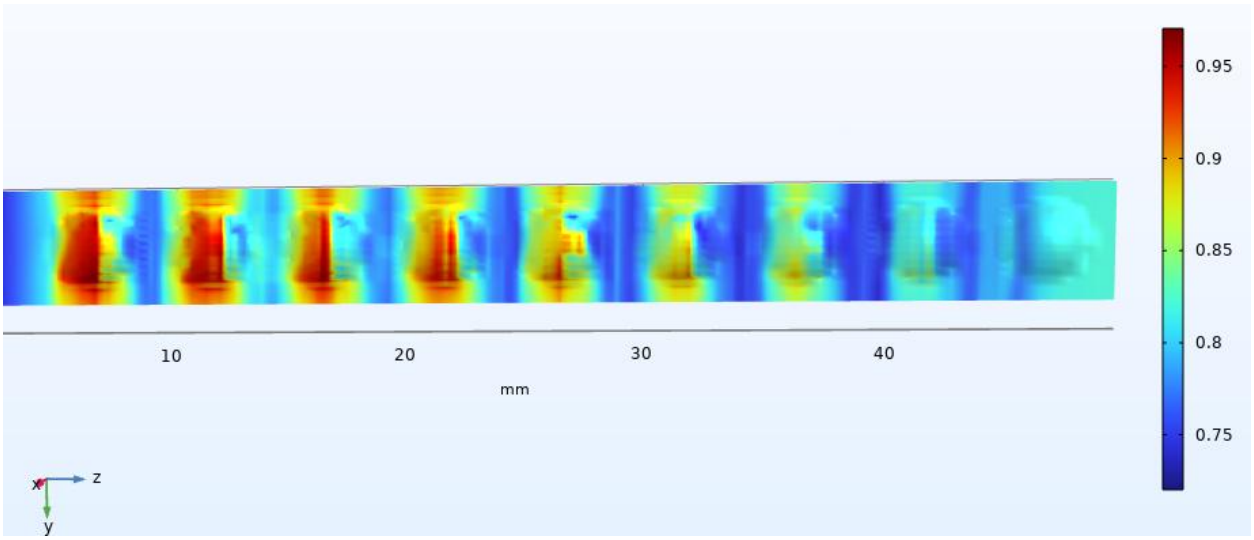


Figure 3.29. Normalized surface concentration (colour bar) on the catalyst film at the 100th unit cell. Re = 1796 and I = 122 W m^{-2}.

Based on Figure 3.27, there is a slight increase in the total consumption over the pass of the SECP reactor compared to the baseline. The intensity and Reynolds trend follows what was observed in the baseline case. The surface concentration of phenol given in Figure 3.28 and Figure 3.29 varies based on the radiation profile shown in Figure 3.23. Higher phenol concentration is observed where the radiation flux was predicting a low rate of absorbed photons due to the shadowing. Under a higher illumination as shown in Figure 3.29 the mass transfer limits become more prominent. It is difficult to say whether mass transfer augmentation in the dimples was augmented under this laminar flow. It appears that the deep dimples may have been less beneficial overall for the radiation field since there are now more regions of lower photon flux. This motivates future geometrical optimization potentially trying to use shallower dimples to yield a more favorable radiation field. The overall augmentation in the rate is most likely due to higher surface area for the catalytic reaction to proceed on.

4 Conclusions

In this work, intrinsic kinetic parameters were fit to a light-dependent LH model by sufficiently decoupling the mass and radiation dependencies. The kinetic parameters obtained through nonlinear least squares regression had excellent agreement with the experimental data from the flat plate photoreactor. Oxygen was found to have a negligible adsorption coefficient, which motivated a first-order reduction in the rate law. The linear dependence on the LASREA was found to fit the entire range of low intensities studied well. The use of a flow distributor near the reaction zone is not recommended as it skewed the laminar flow predictions away from the 1/3 scaling expected from theory. This loss of laminar behaviour was most likely caused by increased turbulence near the film due to potential pore jets created by the packed bed.

For future kinetic experiments, if the goal is to examine the effect of varying flow on a new test geometry while retaining the ability to estimate intrinsic kinetics, then it is recommended to use a slow laminar flow without disturbances to ensure an easily predictable flow field. This would allow the use of either known literature data or easily computable CFD modelling to decouple the mass transport effects with high accuracy. Otherwise, it is better to have a prior estimate of intrinsic kinetics from literature or via a highly agitated bench-scale study where mass transfer effects can be eliminated. Future improvements to this model experimentally could be done by testing a larger range of intensities. This would allow for a more accurate prediction of when the transition from the photon flux limit to the mass transfer limits. Moreover, degradation data at intensities larger than 200 W m^{-2} could be used to determine the photon flux required for the rate to scale sublinearly.

The second objective of this work was accomplished by using the extracted intrinsic kinetic parameters to model a triangular duct and a novel SECP geometry. CFD was used to model the flow and mass transport for moderately sized cavities and protrusions. A rigorous and efficient computational workflow with the capability of coupling the hydrodynamic modelling and radiation modelling via ray tracing was achieved using COMSOL Multiphysics. Using a depth-to-diameter ratio of 0.2 created low-flow recirculation zones from the bulk fluid on the dimple based SECP. The flow followed the curvature of the protrusions under the range of laminar flows examined. Significant shadowing caused by this deep cavity/large protrusion caused localized hotspots and regions of low photon flux, which is detrimental overall to performance. A higher degradation rate was observed overall but it is more likely due to the slightly higher catalyst surface area.

Future work on the SECP geometry is mainly rooted in geometrical optimization. Only a single baseline case was presented in this work, but several geometrical parameters, including the pitch, cavity/protrusion height, array positions, and number of unit cells, could be optimized to yield the best mass transfer improvement while decreasing shadowing caused by the surface modifications. Solving the full combined model for the protrusion flow could also be beneficial. Modelling the full solar distribution would also be beneficial to see how the hotspots in the radiation field change over a full day of sunlight. Extension into turbulent flow modelling for this geometry would also be valuable since mass transfer enhancement could be achieved with lower pressure drops.

5 References

[1] M. Janczarek, E. Kowalska, Computer Simulations of Photocatalytic Reactors, Catalysts 11 (2021) 198. https://doi.org/10.3390/catal11020198.

[2] J.R. García, M.D.L.M. Ballari, Two-dimensional model in a laminar flow slit photoreactor for the determination of surface kinetic constants considering the presence of diffusion limitations, Chemical Engineering Science 300 (2024) 120537. https://doi.org/10.1016/j.ces.2024.120537.

[3] A.T. Nguyen, R.-S. Juang, Photocatalytic degradation of p-chlorophenol by hybrid H2O2 and TiO2 in aqueous suspensions under UV irradiation, Journal of Environmental Management 147 (2015) 271–277. https://doi.org/10.1016/j.jenvman.2014.08.023.

[4] Q. Jamil, B. Žener, U. Putar, L. Matoh, Continuous flow photocatalytic reactor for degradation of selected pollutants: Modeling, kinetics, mineralization rate, and toxicity assessment, Heliyon 10 (2024) e40019. https://doi.org/10.1016/j.heliyon.2024.e40019.

[5] A.L.T. Zheng, A.E. Sinin, W.T. Jin, K.L. Feng, S. Boonyuen, E.L.T. Chung, J. Lease, Y. Andou, Rare earth elements for enhancing photocatalysis in pollutant degradation and water treatment, Int. J. Environ. Sci. Technol. 22 (2025) 7247–7270. https://doi.org/10.1007/s13762-024-06203-5.

[6] Y. Yang, H. Khan, S. Gao, A.K. Khalil, N. Ali, A. Khan, P.L. Show, M. Bilal, H. Khan, Fabrication, characterization, and photocatalytic degradation potential of chitosan-conjugated manganese magnetic nano-biocomposite for emerging dye pollutants, Chemosphere 306 (2022) 135647. https://doi.org/10.1016/j.chemosphere.2022.135647.

[7] M. Sharma, B.S. Kumar, R. Chandrashekar, G. Nijhawan, C. Muralikrishna, M.I. Habelalmateen, R. Goyal, B. Patnaik, Modern Approaches in Water Treatment: Emerging Technologies and Future Directions, E3S Web Conf. 596 (2024) 01046. https://doi.org/10.1051/e3sconf/202459601046.

[8] N. Khodabandeh Lu, H. Alamdari, H. Rashedi, F. Yazdian, M. Pourmadadi, A. Rahdar, L.F. Romanholo Ferreira, Photocatalytic Bioreactors in Water Treatment: Mechanisms, Challenges, and Innovations in Microbial Inactivation, Water Air Soil Pollut 236 (2025) 312. https://doi.org/10.1007/s11270-025-07919-x.

[9] L. Liu, Z. Shen, C. Wang, Recent advances and new insights on the construction of photocatalytic systems for environmental disinfection, Journal of Environmental Management 353 (2024) 120235. https://doi.org/10.1016/j.jenvman.2024.120235.

[10] M.N. Chong, B. Jin, C.W.K. Chow, C. Saint, Recent developments in photocatalytic water treatment technology: A review, Water Research 44 (2010) 2997–3027. https://doi.org/10.1016/j.watres.2010.02.039.

[11] J. Zhang, B. Tian, L. Wang, M. Xing, J. Lei, Photocatalysis: Fundamentals, Materials and Applications, Springer Singapore, Singapore, 2018. https://doi.org/10.1007/978-981-13-2113-9.

[12] C. Casado, J. Marugán, R. Timmers, M. Muñoz, R. Van Grieken, Comprehensive multiphysics modeling of photocatalytic processes by computational fluid dynamics based on intrinsic kinetic parameters determined in a differential photoreactor, Chemical Engineering Journal 310 (2017) 368–380. https://doi.org/10.1016/j.cej.2016.07.081.

[13] J. Yu, ed., S-scheme heterojunction photocatalysts: fundamentals and applications, Academic Press, London, United Kingdom San Diego, CA, 2023.

[14] J. Zhao, X. Meng, Experimental analysis of a slant perforated mesh-plate photoreactor for water detoxification, Chemosphere 315 (2023) 137782. https://doi.org/10.1016/j.chemosphere.2023.137782.
[15] J. Zhao, G. Ren, Z. Li, X. Meng, Design and experimental analysis of a novel slant-plate photoreactor, AIChE Journal 69 (2023) e17883. https://doi.org/10.1002/aic.17883.
[16] Z. Zhang, W. Anderson, M. Mooyoung, Experimental analysis of a corrugated plate photocatalytic reactor, Chemical Engineering Journal 99 (2004) 145–152. https://doi.org/10.1016/j.cej.2004.01.001.
[17] Z. Zhang, W.A. Anderson, M. Moo-Young, Modeling of corrugated plate photocatalytic reactors and experimental validation, Chemical Engineering Science 58 (2003) 911–914. https://doi.org/10.1016/S0009-2509(02)00624-3.
[18] N. Qi, H. Zhang, B. Jin, K. Zhang, CFD modelling of hydrodynamics and degradation kinetics in an annular slurry photocatalytic reactor for wastewater treatment, Chemical Engineering Journal 172 (2011) 84–95. https://doi.org/10.1016/j.cej.2011.05.068.
[19] V. Vaiano, O. Sacco, D. Pisano, D. Sannino, P. Ciambelli, From the design to the development of a continuous fixed bed photoreactor for photocatalytic degradation of organic pollutants in wastewater, Chemical Engineering Science 137 (2015) 152–160. https://doi.org/10.1016/j.ces.2015.06.023.
[20] D. Chen, F. Li, A.K. Ray, External and internal mass transfer effect on photocatalytic degradation, Catalysis Today 66 (2001) 475–485. https://doi.org/10.1016/S0920-5861(01)00256-5.
[21] Z. Zhang, Analysis of a corrugated plate photocatalytic reactor, University of Waterloo, 1999.
[22] I. Grčić, N. Koprivanac, G. Li Puma, Modeling the photocatalytic oxidation of carboxylic acids on aqueous TiO2 suspensions and on immobilized TiO2-chitosan thin films in different reactor geometries irradiated by UVA or UVC light sources, Chemical Engineering Journal 422 (2021) 130104. https://doi.org/10.1016/j.cej.2021.130104.
[23] N.A.B. Timmerhuis, J.A. Wood, R.G.H. Lammertink, Connecting experimental degradation kinetics to theoretical models for photocatalytic reactors: The influence of mass transport limitations, Chemical Engineering Science 245 (2021) 116835. https://doi.org/10.1016/j.ces.2021.116835.
[24] S. Corbel, N. Becheikh, T. Roques-Carmes, O. Zahraa, Mass transfer measurements and modeling in a microchannel photocatalytic reactor, Chemical Engineering Research and Design 92 (2014) 657–662. https://doi.org/10.1016/j.cherd.2013.10.011.
[25] M.D.L.M. Ballari, O.M. Alfano, A.E. Cassano, Mass transfer limitations in slurry photocatalytic reactors: Experimental validation, Chemical Engineering Science 65 (2010) 4931–4942. https://doi.org/10.1016/j.ces.2010.04.021.
[26] G.I. Mahmood, P.M. Ligrani, Heat transfer in a dimpled channel: combined influences of aspect ratio, temperature ratio, Reynolds number, and flow structure, International Journal of Heat and Mass Transfer 45 (2002) 2011–2020. https://doi.org/10.1016/S0017-9310(01)00314-3.
[27] H. Qu, Z. Shen, Y. Xie, Numerical Investigation of Flow and Heat Transfer in a Dimpled Channel among Transitional Reynolds Numbers, Mathematical Problems in Engineering 2013 (2013) 1–10. https://doi.org/10.1155/2013/989237.

[28] A. Ebrahimi, B. Naranjani, An investigation on thermo-hydraulic performance of a flat-plate channel with pyramidal protrusions, Applied Thermal Engineering 106 (2016) 316–324. https://doi.org/10.1016/j.applthermaleng.2016.06.015.
[29] M.G. Rasul, S. Ahmed, M.A. Sattar, M.I. Jahirul, Hydrodynamic performance assessment of photocatalytic reactor with baffles and roughness in the flow path: A modelling approach with experimental validation, Heliyon 9 (2023) e19623. https://doi.org/10.1016/j.heliyon.2023.e19623.
[30] T. Rath, J.Z. Bloh, A. Lüken, K. Ollegott, M. Muhler, Model-Based Analysis of the Photocatalytic HCl Oxidation Kinetics over TiO_2, Ind. Eng. Chem. Res. 59 (2020) 4265–4272. https://doi.org/10.1021/acs.iecr.9b05820.
[31] A. Mills, J. Wang, Photomineralisation of 4-chlorophenol sensitised by TiO2 thin films, Journal of Photochemistry and Photobiology A: Chemistry 118 (1998) 53–63. https://doi.org/10.1016/S1010-6030(98)00361-X.
[32] M.L. Satuf, R.J. Brandi, A.E. Cassano, O.M. Alfano, Modeling of a Flat Plate, Slurry Reactor for the Photocatalytic Degradation of 4-Chlorophenol, International Journal of Chemical Reactor Engineering 5 (2007). https://doi.org/10.2202/1542-6580.1539.
[33] Z. Zhang, W.A. Anderson, M. Moo-Young, Rigorous modeling of UV absorption by TiO_2 films in a photocatalytic reactor, AIChE Journal 46 (2000) 1461–1470. https://doi.org/10.1002/aic.690460719.
[34] E. Shashi Menon, Chapter Five - Fluid Flow in Pipes, in: Transmission Pipeline Calculations and Simulations Manual, Gulf Professional Publishing, Boston, 2015: pp. 149–234. https://doi.org/10.1016/B978-1-85617-830-3.00005-5.
[35] R.K. Shah, A.L. London, Laminar flow forced convection in ducts: a source book for compact heat exchanger analytical data, Academic Press, New York, 1978.
[36] Y.S. Muzychka, M.M. Yovanovich, Laminar Forced Convection Heat Transfer in the Combined Entry Region of Non-Circular Ducts, Journal of Heat Transfer 126 (2004) 54–61. https://doi.org/10.1115/1.1643752.
[37] IAPWS, International Association for the Properties of Water and Steam, "Release on the IAPWS Formulation 2008 for the Viscosity of Ordinary Water Substance, (2008). http://www.iapws.org/relguide/viscosity.html.
[38] IAPWS, International Association for the Properties of Water and Steam, IAPWS R6-95, Revised Release on the IAPWS Formulation 1995 for the Thermodynamic Properties of Ordinary Water Substance for General and Scientific Use, (2016). http://www.iapws.org/relguide/IAPWS-95.html.
[39] R.B. Bird, W.E. Stewart, E.N. Lightfoot, D.J. Klingenberg, Introductory transport phenomena, Wiley, Hoboken, NJ, 2015.
[40] L.F.G. Martins, M.C.B. Parreira, J.P.P. Ramalho, P. Morgado, E.J.M. Filipe, Prediction of diffusion coefficients of chlorophenols in water by computer simulation, Fluid Phase Equilibria 396 (2015) 9–19. https://doi.org/10.1016/j.fluid.2015.03.026.
[41] W.M. Haynes, ed., CRC Handbook of Chemistry and Physics, 95th ed., CRC Press, 2014. https://doi.org/10.1201/b17118.
[42] COMSOL Multiphysics® v. 6.4.0.293, Reference Manual, (2026).
[43] R9-97: Release on the Refractive Index of Ordinary Water Substance as a Function of Wavelength, Temperature and Pressure, (n.d.). https://iapws.org/documents/release/Rindex (accessed August 10, 2026).

[44] B.W. Rust, Fitting Nature's Basic Functions Part III: Exponentials, Sinusoids and Nonlinear Least Squares, Computing in Science & Engineering 4 (2002). https://www.nist.gov/publications/fitting-natures-basic-functions-part-iii-exponentials-sinusoids-and-nonlinear-least (accessed August 8, 2026).
[45] least_squares — SciPy v1.16.1 Manual, (n.d.). https://docs.scipy.org/doc/scipy/reference/generated/scipy.optimize.least_squares.html#scipy.optimize.least_squares (accessed September 1, 2025).
[46] T.L. Bergman, A.S. Lavine, Fundamentals of heat and mass transfer, Eighth edition, John Wiley & Sons, Hoboken, NJ, 2017.
[47] J. Von Seckendorff, N. Szesni, R. Fischer, O. Hinrichsen, Experimental characterization of random packed spheres, cylinders and rings, and their influence on pressure drop, Chemical Engineering Science 222 (2020) 115644. https://doi.org/10.1016/j.ces.2020.115644.
[48] S. Bu, J. Yang, Q. Dong, Q. Wang, Experimental study of transition flow in packed beds of spheres with different particle sizes based on electrochemical microelectrodes measurement, Applied Thermal Engineering 73 (2014) 1525–1532. https://doi.org/10.1016/j.applthermaleng.2014.03.063.
[49] M. Ahtasham Iqbal, S. Akram, S. Khalid, B. Lal, S.U. Hassan, R. Ashraf, G. Kezembayeva, M. Mushtaq, N. Chinibayeva, A. Hosseini-Bandegharaei, Advanced photocatalysis as a viable and sustainable wastewater treatment process: A comprehensive review, Environmental Research 253 (2024) 118947. https://doi.org/10.1016/j.envres.2024.118947.
[50] A.V. Emeline, V. Ryabchuk, N. Serpone, Factors affecting the efficiency of a photocatalyzed process in aqueous metal-oxide dispersions, Journal of Photochemistry and Photobiology A: Chemistry 133 (2000) 89–97. https://doi.org/10.1016/S1010-6030(00)00225-2.
[51] S.J. Armaković, M.M. Savanović, S. Armaković, Titanium Dioxide as the Most Used Photocatalyst for Water Purification: An Overview, Catalysts 13 (2022) 26. https://doi.org/10.3390/catal13010026.

6 Appendix – Meshing Strategies

This appendix serves to outline the mesh strategies for each case presented.

6.1 Baseline Case

To allow for a structured mapped quad mesh on the triangular duct, the bottom tip of the triangular duct was truncated to create the 4 sides needed to fit quad cells within the geometry. 1 mm was chosen since it takes up less than 10% of the total hydraulic diameter on the sharpest-angle duct. Moreover, it is within the region of lowest flow, so truncation to ensure a better mesh quality can be done without disrupting the physical flow structures of interest. Figure 3.11 confirms this by plotting the velocity profile in the overall bulk flow of the duct compared to its analytical approximation.

The meshing strategy for the fully developed flow is simple. Element grading closer to the walls is done where the velocity gradients are high. There is no need for axial refinement since the flow does not change axially when fully developed. Figure 6.1 shows the final mesh which gave the velocity profile of Figure 3.11 and was unchanging with additional refinement.

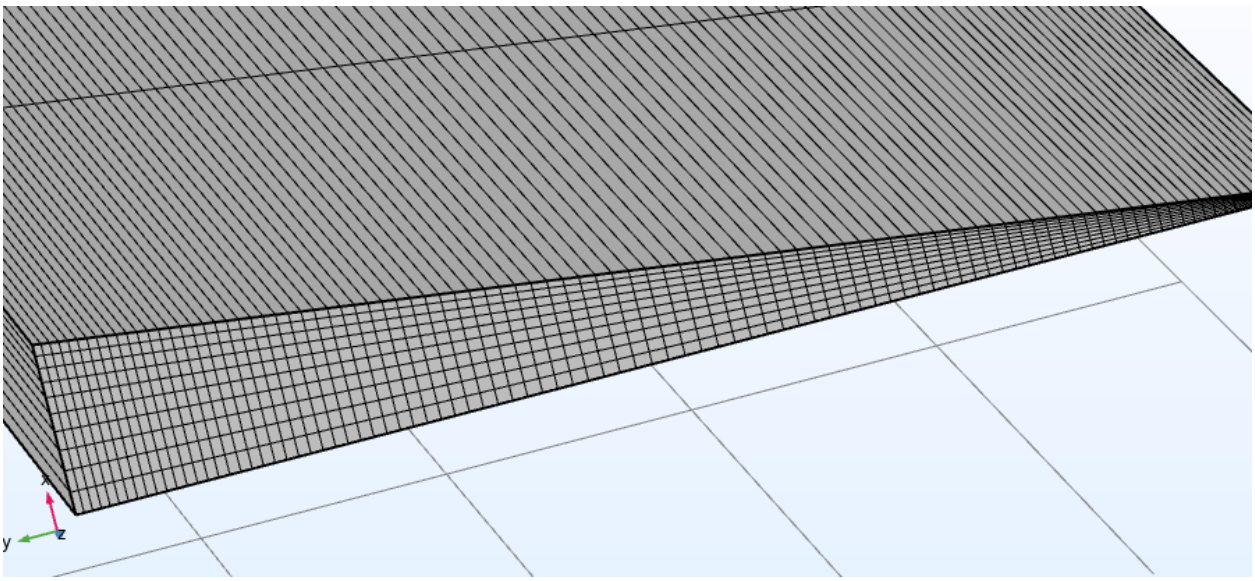


Figure 6.1. Structured quad mesh on the baseline geometry suitable for computing the laminar flow field.

The strategy for the mesh refinement for the mass transfer required more careful consideration. The mass boundary layer for 4-CP is very thin due to its low diffusivity. As such, to fully resolve the concentration gradient, enough cells need to be within that thin layer. Moreover,

the concentration boundary layer develops axially with the flow. The strategy was as follows. Run a base case using the resolved flow mesh. Estimate the thickness of the concentration boundary layer by plotting the concentration profile normal to the reactive surface. Bias more cells closer to this thin layer and compute the average mass transfer coefficient using the normal diffusive flux and the bulk concentration. Add more cells axially and bias them towards the reactor entrance. Convergence is reached once the average mass transfer coefficient along the entire reactor length ceases to change. The final mesh is shown in Figure 6.2. The average mass transfer coefficient for the highest case run (Re = 1700) is shown in Figure 6.3.

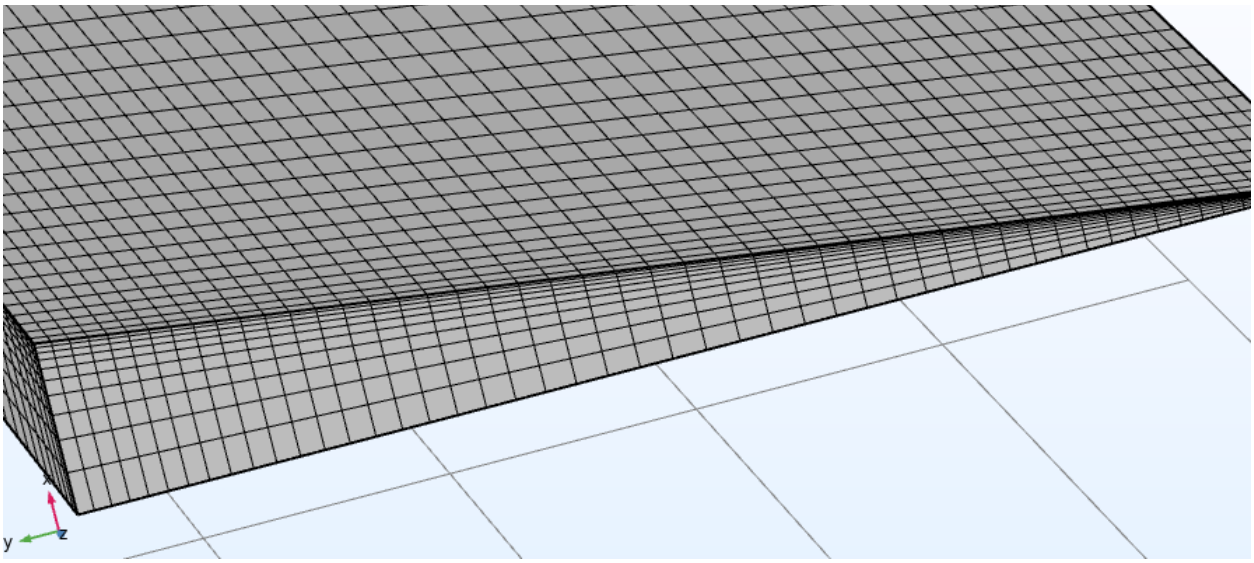


Figure 6.2. Structured quad mesh on the baseline geometry suitable for resolving the diffusion boundary layer.

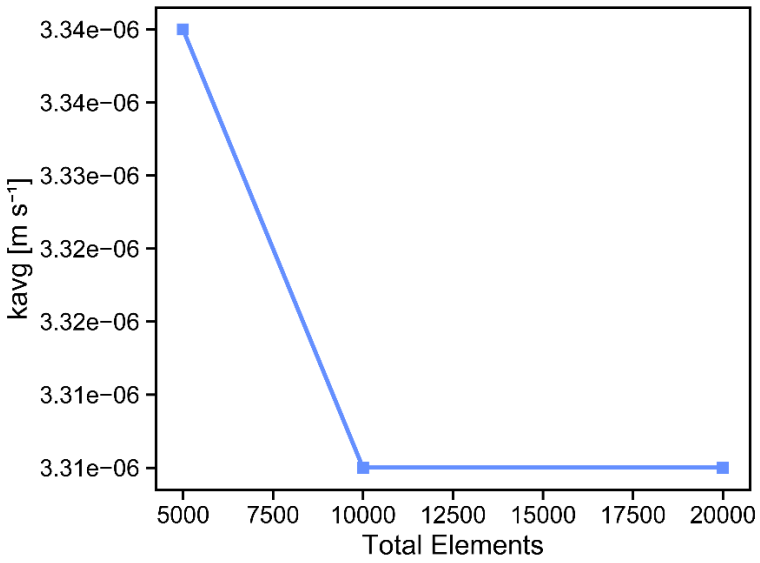


Figure 6.3. Mesh refinement plot for the average 4-CP mass transfer coefficient on the baseline geometry under the highest Re of 1700.

The average mass transfer coefficients are then compared to the Muzychka and Yovanovich [36] model for validation. The results of this are shown in Figure 6.4, all of which are within 6-7%, which is within the $\pm 10\%$ model range.

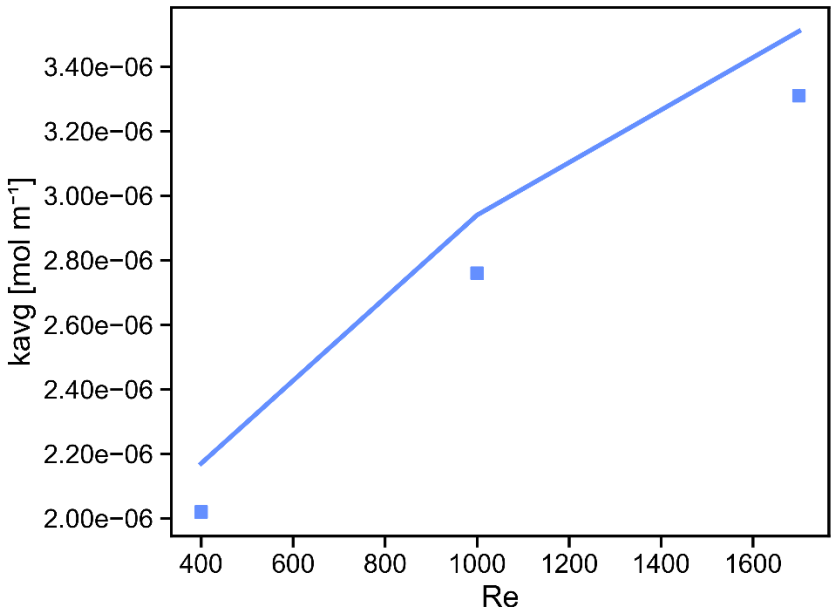


Figure 6.4. 4-CP average mass transfer coefficient compared to the Muzychka and Yovanovich model.

6.2 SECP

To create a structured mesh on the dimple surface while keeping a smooth representation of the dimple lip, multiple mesh techniques were used. Mesh deformation was used to create the dimples while curving the mesh lines to follow the rounded structure. This is a COMSOL workaround to create a body-fitted mesh on curvilinear coordinates. Another advantage is the large increase in cell quality compared to using inflation layers around the lip. Due to the high angle created by the duct and the dimple (at higher depth-to-diameter ratios), the inflation stack must be trimmed near the lip, which causes very poor cell quality around a region of high importance. Mapped quad meshing was done on the main volume and swept. Partitioning of the domain was done to allow for higher refinement near the dimples. The refinement included: higher wall-normal cells to capture the thin boundary layers and a higher number of surface cells to adequately create the curved surface with minimal faceting. Mesh deformation is a very good use case for fluid flow but not so much for radiation modelling, where the curvature of the geometry matters to determine reflection angles. Using an unstructured mesh might end up being better for this use case.

To track mesh independence for the flow in the SECP dimples cavity exchange flow, the size of the recirculation zone was tracked. As the mesh was refined from 1250 to 10000 to 40000 quadratic elements the cavity exchange flow (i.e. the how much of the bulk flow enters the cavities) only changed by at most 3.5%. This was deemed acceptable for accuracy, while maintaining a reasonable compute time. The recirculation volume was tracked estimating the volume with a reverse flow sign. Under the same mesh refinement study the relative error for the recirculation zone size for the highest Reynolds number of 1796 is given by Figure 6.5. The volume only changing by 10% was deemed acceptable.

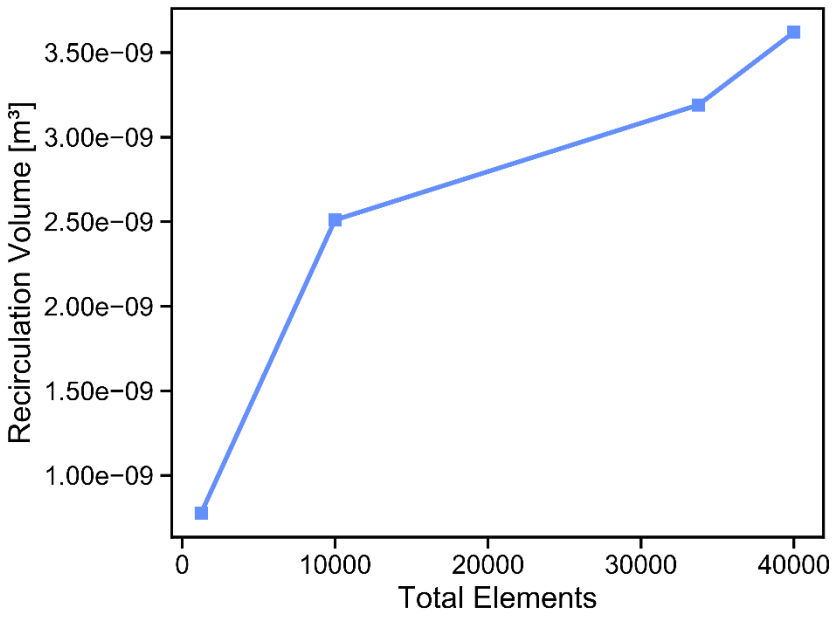


Figure 6.5. Mesh convergence plot for the recirculation volume within all the dimples modelled in the SECP reactor.

The converged mesh for the flow is given by Figure 6.6. Likewise; the mass transfer mesh biased many cells to ensure the mass boundary layer is well resolved. This is given by Figure 6.7.

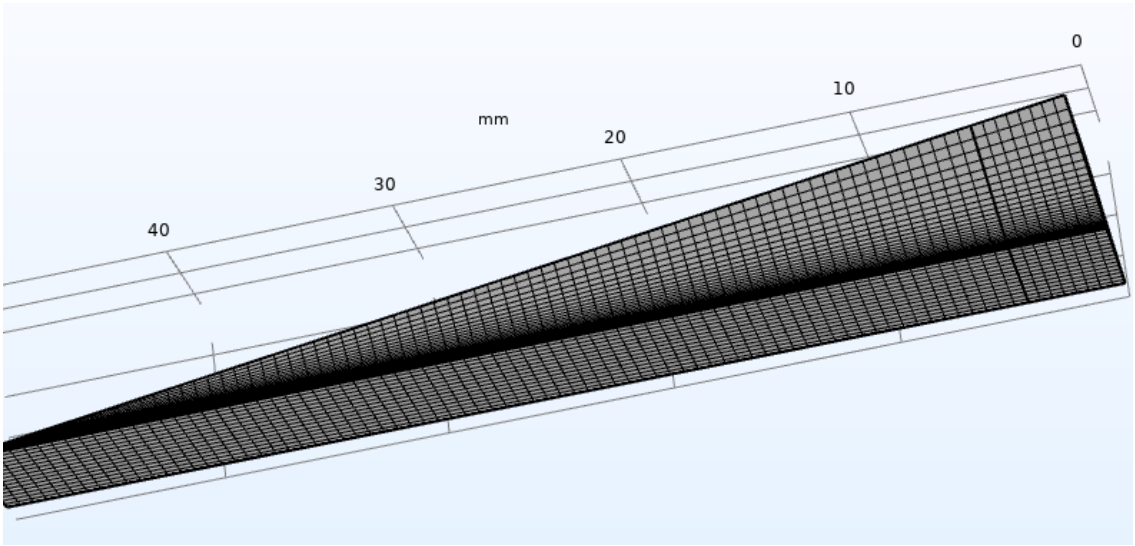


Figure 6.6. Flow mesh for the SECP

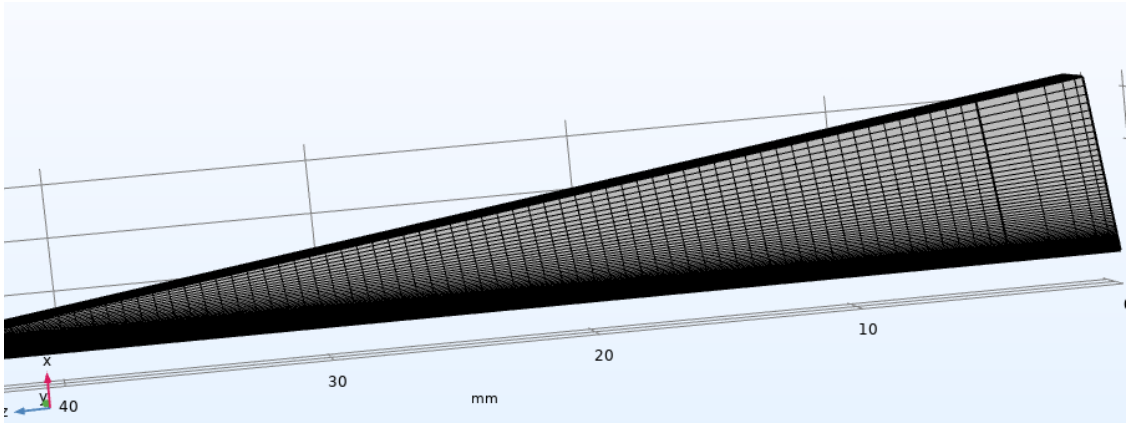


Figure 6.7. Mass transfer mesh for SECP